



HAL
open science

Zinc-rich clays in supergene non-sulfide zinc deposits

Flavien Choulet, M. Buatier, Luc Barbanson, Régis Guégan, A. Ennaciri

► **To cite this version:**

Flavien Choulet, M. Buatier, Luc Barbanson, Régis Guégan, A. Ennaciri. Zinc-rich clays in supergene non-sulfide zinc deposits. *Mineralium Deposita*, 2016, 51 (4), pp.467-490. 10.1007/s00126-015-0618-8. insu-01239887

HAL Id: insu-01239887

<https://insu.hal.science/insu-01239887>

Submitted on 10 Dec 2015

HAL is a multi-disciplinary open access archive for the deposit and dissemination of scientific research documents, whether they are published or not. The documents may come from teaching and research institutions in France or abroad, or from public or private research centers.

L'archive ouverte pluridisciplinaire **HAL**, est destinée au dépôt et à la diffusion de documents scientifiques de niveau recherche, publiés ou non, émanant des établissements d'enseignement et de recherche français ou étrangers, des laboratoires publics ou privés.



Distributed under a Creative Commons Attribution - NonCommercial - NoDerivatives 4.0 International License

Zinc-rich clays in supergene non-sulfide zinc deposits.

1 “Fertilization” of barren clays in supergene non-sulphide zinc deposits

2

3 Choulet F.^{1,*}, Buatier M.², Barbanson L.², Guégan R.², Ennaciri A.³

4

5 ¹: Chrono-Environnement, Université de Franche-Comté/CNRS (UMR6249), Besançon, France

6 ²: ISTO, Université d'Orléans/CNRS (UMR7327), Orléans, France

7 ³: Groupe Managem, Casablanca, Morocco

8 * : **corresponding author** flavien.choulet@univ-fcomte.fr

9

10 **Abstract**

11

12 The nature and the origin of zinc clays are poorly understood. Based on the example of the
13 Bou Arhous Zn-Pb ore deposit in the Moroccan High Atlas, this study presents new advances for the
14 characterization of barren and mineralised clays associated to zinc non-sulphide ores. In the field, white
15 to ochre granular clays are associated with willemite, whilst red smooth clays fill karst-related cavities
16 cutting across the non-sulphide ore bodies. Red clays (kaolinite chlorite, illite and smectite) present
17 evidence of stratification that reflects internal sedimentation processes during karst evolution. White
18 clays contain 7Å-clay mineral/smectite irregular mixed layers with less than 20% of smectite layers.
19 The willemite crystals are partially dissolved and are surrounded by authigenic zinc clay minerals.
20 WDS analyses on newly formed clay aggregates have revealed that this mixed layered mineral is
21 composed by fraipontite and sauconite. CEC measurements support that zinc is only located within the
22 octahedral sheets. These new results support the following process: 1) dissolution of willemite, leading
23 to releasing Si and Zn, 2) interaction between Zn-Si rich solutions and residual-detrital clays, 3)
24 neogenesis of mixed-layered zinc clay minerals that grow over detrital micas, ~~representing~~ the source
25 for Al.

26

27 **Keyword:** supergene zinc deposits, karst, clay minerals, Morocco

28

29 **1) Introduction**

30

31 Clays are often considered to be a knotty challenge for ore processing (**Connelly 2011; Lim**
32 **2011**), because of their size and shape characteristics. The typical problems met by the mining industry
33 encompass the difficulties of handling, crushing, screening, milling and classifying clay-rich raw
34 material. High grade of clay results in poor selectivity and thus significantly slow flotation kinetics
35 (e.g. **Bayraktar et al. 1998; Fuerstenau et al. 2007**). Occurrence of clays in the ore may also affect
36 leaching techniques by increasing pulp viscosity. Despite many efforts to fathom these crucial
37 difficulties, cost of solutions is considerable and hence clays act as a brake on ore extraction and
38 processing. Another difficulty with clays associated to ores is their potential to trap metal (**Newman**
39 **1987**). Hence a noteworthy amount of economic elements is captured in clays, which are often difficult
40 to process for recovery (e.g. Ni-rich clays, **Crundwell et al. 2011**). Understanding the nature and the
41 origin of clays associated to ores is critical for designing flowsheet and identifying potential
42 unconventional sources for critical metal extraction and recovery.

43 Recent development of coupled techniques of leaching, solvent extraction and electrowinning
44 and their application to zinc smelting (**Gnoinski 2006; de Wet and Singleton 2008; Abkhoshk et al.**
45 **2014**) have contributed to revive interest in the disregarded non-sulphide deposits with successful
46 application in Namibia, Peru and Morocco. Supergene non-sulphide zinc deposits are formed during
47 weathering in relation with tectonics and climate (**Hitzman et al. 2003**). Such deposits are described
48 around the world and occur in various geological environments, from silicoclastic to carbonate host
49 rocks (**Boni and Large 2003**). Based on genetic processes at their origin, three types of supergene
50 deposits have been distinguished: 1) direct-replacement deposits, 2) wall-rock deposits and 3) karst-
51 filling deposits (**Hitzman et al. 2003**). These different processes may occur together in a given deposit,
52 affecting the texture of ores and providing an intricate mineralogical record. This includes carbonates
53 (smithsonite), hydrated carbonates (hydrozincite), silicates (willemite), hydrated silicates
54 (hemimorphite) and various rare minerals, including clays such as sauconite, a smectite containing up
55 to 50 %wt of ZnO (**Ross 1946**) or more rarely fraipontite, a zinc bertherine (**Fransolet and**
56 **Bourguignon 1975**).

57 In many supergene zinc deposits, mineralised clay material represents a significant economic
58 resource that cannot be ignored (e.g. up to 30 % of the ore at Accha in Peru, **Boni et al. 2009a**). The
59 occurrence of such amount of clays in the ore requires desliming and results in lower zinc recovery (**de**
60 **Wet and Singleton 2008**), although the impact of clays is probably lower than expected from

61 mineralurgical tests (**Boni et al. 2009b**). Besides, the ability of clays to sorb or catch Zn^{2+} cations
62 located within the interlayer space of swelling clays is well known (**Bradbury and Baeyens 1999**;
63 **Churakov and Dähn 2012**), implying natural clays may represent an economic potential of zinc
64 recovery without much efforts. Although zinc enriched clays are frequently described in supergene
65 deposits, clear identification of the nature of clay minerals remains rare and the classical sauconite
66 assessment is highly speculative. In addition, the origin of zinc clays and its place within the ore
67 evolution remain badly understood.

68 This study investigates the characterisation of zinc clays of the Bou Arhous deposit in the
69 Moroccan High Atlas. This deposit is hosted in Lower Jurassic limestone, and ore is mainly willemite,
70 whose origin is not clearly understood (**Choulet et al. 2014**). Willemite is associated to various types
71 of clayey material, presenting differences in mineralogy, texture and Zn content. The Bou Arhous ore
72 deposit represents a key natural example to understand the origin of zinc-bearing clays and their place
73 in the ore deposition. Using microscopic observations and classical techniques for investigating clay
74 minerals, we aim at characterizing the nature of clays recorded at Bou Arhous and debate on their
75 origin. Further quantification of the cation exchange capacity (CEC) allows us to discuss the potential
76 of zinc recovery.

77

78 **2) Geological setting of the Bou Arhous ore deposit**

79

80 The Bou Arhous Pb-Zn ore deposit (32.27°N, 3.76°W) is located in the Moroccan High Atlas
81 range, 60 km to the north-east of Errachidia city (**Fig. 1A**). The local geology of this deposit has been
82 extensively studied by Leblanc (**1968**) and recently revisited in Choulet et al. (**2014**).

83 The formation of the High Atlas intra-continental fold-and-thrust belt (**Mattauer et al. 1977**)
84 results from the far-field effect of the Alpine collision events since mid-Tertiary (ca. 40 Ma) and up to
85 Pleistocene (**Frizon de Lamotte et al. 2009**). As a consequence, the Mesozoic sedimentary basins
86 formed during the opening of Tethys and Atlantic Oceans have been affected by inversion tectonics
87 accompanied by regional uplift and localized exhumation of Lower Jurassic and Triassic strata in the
88 core of narrow anticlines. Thereafter, exhumed strata experienced surface weathering leading to the
89 karst development in the Jurassic limestone (**Choulet et al. 2014; Charles et al. submitted**).

90 The Jbel Bou Arhous range is one of these ENE-WSW trending faulted anticlines that exhume
91 the Triassic and Lower Jurassic strata (**Fig. 1B**). The fold-related “Grand Accident” thrust is rooted in
92 the Triassic substratum (**Figs. 1B and 1C**; **Teixell et al. 2003**) and represents a reactivated normal fault
93 that delimited contrasting paleogeographic domains of the former Tethys Sea (**Warne 1998**). To the
94 north of the fault, deep-seated dolomitic limestone is almost barren, whereas massive limestone of the
95 southern domain originally deposited in reef or para-reef environments includes lenses of base metal
96 sulphides (**Figs. 1B and 1C**). At site of the Bou-Arhous mine located in the footwall of the “Grand
97 Accident” thrust, the two limbs of the anticline are vertical (**Fig. 2A**) or slightly recumbent and the fold
98 hinge is missing (**Fig. 1C**). Host rocks of mineralisation include Sinemurian black limestone, locally
99 interbedded with thin layers of greyish marls (**Fig. 2B**), which have experienced slight dolomitisation
100 during diagenesis and emplacement of base metals sulphide lenses (**Leblanc 1968**). In depth,
101 mineralisation is tectonically juxtaposed along the “Grand Accident” thrust to the Triassic variegated
102 shales associated to gypsum (**Fig. 2C**).

103 Following exploration campaigns in the 1960’s, the Bou Arhous mine has been exploited by
104 Managem since the early 2000’s and reserves have been estimated at 250 kt grading 4 % Pb and 16 %
105 Zn. Mineralisation consists of an intricate network of various-sized veins, extending over 18000 square
106 metres. Veins up to 10 metres in width parallel the stratification and dip steeply to the north (**Fig. 2A**).
107 Non-sulphide zinc-bearing minerals include willemite, hydrozincite, hemimorphite and smithsonite.
108 Gangue minerals include automorphous white carbonates, such as calcite and dolomite (**Fig. 2D**),
109 emplaced during the early sulphide stage (**Choulet et al. 2014**). Willemite is finely associated to galena
110 remnant and cerussite, forming a well-defined black ore. Black ore generally occurs as disseminated
111 patches enclosed in very fine-grained clay-rich material (**Fig. 2E**), showing a variety of colours. Hence,
112 different types of clayey material have been distinguished and they are detailed in the following
113 section.

114

115 **3) The different types of clay deposits at Bou Arhous**

116

117 Previous investigation of the clayey material associated to the mineralisation (**Leblanc 1968**)
118 suggested the existence of two types of clays. Reddish and smooth clays occur as infilling material of
119 the karstic cavities and were considered of detrital origin as evidenced by the layering structures. These

120 clays are barren, but they locally contain some fragments of the non-sulphide mineralisation. In
121 contrast, white and granular clays are frequently associated to willemite and Leblanc (1968) suggested
122 that these clays might correspond to newly formed clay minerals with up to 23 % of Zn (Gaufrey
123 1953).

124 Based on a recent detailed field study, a new examination of the clay materials has been
125 carried out and we now distinguish three types of clayey material, which may coexist in a same area
126 (Fig. 3A).

127 1) Red clayey material fills a network of connected cavities, sinkholes and tunnels, related to the karst
128 of Bou Arhous (Fig. 3B). A sub-horizontal bedding (Fig. 3C) with evidence of grain size sorting is
129 frequently observed, as well as various-sized clastic fragments of ore and host limestone. The aspect of
130 the red clayey material may be locally smooth, but is often silty or sandy due to millimetre-sized quartz
131 grains. This red clayey material corresponds to the reddish and smooth clays described by Leblanc
132 (1968).

133 2) White clayey material occurs as a fine-grained matrix embedding disseminated patches of willemite
134 associated with carbonates and galena. It forms either a thin and partial rim between the black ore and
135 the red clays (Fig. 3D), or a widespread impregnation in the mineralisation (Fig. 3E). The white colour
136 is not systematic and tends to be locally yellowish, indicating a progressive transition to ochre clays. This
137 type partly encompasses the white granular type observed by Leblanc (1968).

138 3) A third type, namely ochre clays has been found as cavity-infilling material (Fig. 3F) or as a mixture
139 of white and red clayey materials (Fig. 3A). Ochre clays share similar features with white clays, such
140 as their association with black ore but this latter one is less preserved than in the case of white clays.
141 Ochre clays may also occur as isolated material without any spatial connection with white and red
142 clays.

143

144 **4) Sampling and methodology**

145

146 *4.1) Bulk chemical composition*

147

148 Fifty-eight rock samples have been collected at Bou Arhous mine and include host-rocks
149 (Triassic shale and Jurassic limestone and marl) and the three types of clayey material (red clays, white

150 clays and ochre clays), listed in **Table 1**. Among them, thirty-four samples have been duplicated for
151 analysing the chemical composition. The chemical composition measurements using acid digestion
152 procedure have been carried out in Managem Group lab, at Marrakech, Morocco. For major elements,
153 0.5 g of a crushed sample (< 200 µm) has been dried and dissolved by fusion at 500°C during 45
154 minutes with 2.5 g of sodium peroxide in a zirconium crucible. The residue was then dissolved in HCl
155 and the solution has been analysed by ICP-AES ULTIMA 2C. For minor elements, a 0.25 g split has
156 been heated (220 °C during 45 minutes) in HCl (50%) – HNO₃ (50%) to fuming and the solution was
157 analysed by ICP-MS Thermo X'Serie 2.

158

159 4.2) Clay fraction study

160

161 In addition, for twenty-two samples, the clay fraction (<2 µm) has been separated by
162 decantation using the following procedure. A rock sample has been crushed using a Retsch PM200 ball
163 mill and manually ground in agate mortar. The rock powder has been dissolved in distilled water and
164 dispersed with a magnetic stirrer. Progressive addition of HCl (0.2M) monitored by continuous pH
165 measurements was used to remove carbonate at room temperature. Then, the solution has been washed
166 several times, dispersed and placed in a jar for decantation. After about 4 hours, the first five
167 centimetres of the solution containing the clay suspension (<2 µm) have been withdrawn using a
168 syringe. After removing the supernatant by centrifugation, the residue has been dried and used for
169 further X-ray diffraction (XRD) and cation-exchange capacity measurements.

170 XRD patterns of the whole rock samples and clay fractions have been obtained using a D8
171 Advance Bruker diffractometer equipped with a LinxEye detector, hosted at Utinam lab, Besancon,
172 France. Parallel beam geometry and CuK α radiation at 1.54184 Å has been used. For whole rock
173 sample, the powder was placed in the specimen holder. Acquisition conditions (divergent slit) included
174 a step-scan of 0.5 ° in the 2-52 ° interval, with a step time of 0.05 s. For the clay fraction, the powder
175 has been diluted in distilled water and a drop of the solution has been deposited on a glass lamella for
176 dewatering under air-dried conditions. The orientated-aggregate mount (along c axis) was then placed
177 in holder and a step-scan of 0.02 ° in the 2-30 ° interval, with a step time of 0.5 s has been used for
178 XRD measurements. A duplicate of the orientated-aggregate mount has been treated for ethylene
179 glycol (EG) saturation, by placing the lamella in a pressurised desiccator overnight. For several

180 samples, a second duplicate has been heated at 550 °C during one hour in a furnace before XRD
181 measurements. EVA software package has been used for data processing and phase identification. The
182 position of 060 reflexion has been determined on clay fraction powders at Institut des Sciences de la
183 Terre d'Orléans, Orléans, France, using an ARL X'TRA diffractometer equipped with Cu anode and a
184 Si solid detector operating at 40 kV and 40 mA. Experimental measurements were carried out at room
185 temperature, with 10 s counting time per 0.02 ° step.

186 Cation-exchange capacity (CEC) measurements have been carried out at the Institut des
187 Sciences de la Terre d'Orléans, Orléans, France following the procedures described in Meier and Kahr
188 (1999) and Ammann et al. (2005). A solution of 0.01M Cu(II)-trien sulphate has been prepared from
189 1.596 g of copper sulphate and 1.508 g of triethylenetetramine. 100+/- 25 mg of clay sample were
190 added to 25 mL of distilled water and to 8 mL of Cu(II)-trien sulphate. The solution has been dispersed
191 using tube roller overnight and was further centrifuged (10 minutes at 6000 rpm) to removed 3 mL of
192 the supernatant. Measurement of [Cu²⁺] was performed using Atomic Absorption Spectroscopy (AAS)
193 with 2-8100 Polarized Zeeman Hitachi instrumentation and colorimetric techniques. The CEC was then
194 calculated with reference to the dry clay weight, to the water content and to the amount of captured
195 Cu²⁺ ions deduced from AAS measurements. A similar procedure is used for calculating the Zn content
196 in the CEC. Standardisation curves of absorbance for [Cu²⁺] and [Zn²⁺] gave coefficients of
197 determination of 0.999 and 0.987, respectively.

198

199 *4.3) Textural and mineralogical observations*

200

201 Textural and mineralogical observations have been carried out using optical microscopy (OM)
202 and FEI Quanta 450 Scanning Electron Microscope (SEM) hosted at Femto-ST lab, Besançon, France.
203 The images have been acquired in low vacuum mode (0.7-0.8 mbar) on polished thin sections, with
204 acceleration voltage at 15 kV. An Energy-Dispersive X-Ray Spectrometer (EDS) was coupled to the
205 SEM system providing qualitative determination of the mineral composition using Edax Genesis
206 software package.

207

208 *4.4) Chemical composition of clay minerals*

209

210 We have performed quantitative analyses using Cameca SX100 electron microprobe (EPMA),
211 equipped with five Wave-Dispersive X-Ray Spectrometers (WDS) and hosted at Géosciences
212 Montpellier, Montpellier, France. On carbon-coated polished thin-section, we have operated at 20 kV
213 with a beam current at 10 nA. The spot resolution was few micrometres. Quantification of the Na
214 content was not possible due to the interference of the Zn L β 1 emission line that fall close to the Na K α
215 emission line.

216

217 **4) Results**

218

219 *4.1) Whole rock geochemical and mineralogical composition*

220

221 *4.1.1) Host rocks*

222 The Triassic shales are composed of a mixture of quartz, clay minerals, hematite, goethite, and
223 carbonates including both calcite and dolomite (**Table 1**). Gypsum is also present in some samples. The
224 major elements content strongly varies due to a variable proportion of carbonates and iron oxi-
225 hydroxides. Variable enrichment in Zn, Pb, Cu and As can be noticed suggesting the local occurrence
226 of sphalerite, galena, and/or other minor metal-bearing minerals.

227 Jurassic rocks including marl and limestone contain clay minerals, calcite, dolomite and
228 quartz (**Table 1**). Goethite is common. The SiO₂ and CaO contents are variable and probably mirror the
229 variable abundance in quartz and carbonate in the samples. Minor elements (Zn, Pb, Cu and As)
230 content remains low except for one sample that contains galena, sphalerite and their respective
231 alteration products.


232

233 *4.1.2) Clayey material*

234 The mineralogy of the red clayey material is characterized by a mixture of quartz, clay
235 minerals, calcite with goethite and rare dolomite (**Table 1**). Despite important variations of CaO and
236 SiO₂ related to carbonate enrichment of some samples (e.g. BA101), the major elements content
237 remains constant. The red clay samples do not display any significant variations of the minor elements
238 content except for Pb and Zn, which display highly variable amounts (e.g. between 830 ppm and 47300

239 ppm for Zn); this could be related to the occurrence of willemite and cerussite impurities in these
240 samples.

241 The white clayey material is composed of a mixture of willemite, galena, quartz, clay minerals
242 and carbonate (dolomite, calcite, and cerussite). Dolomite is almost always observed in white clays,
243 marking a noteworthy difference with red clayey material. The MgO content can therefore reach up to
244 10 %wt (**Table 1**). The occurrence of Zn and Pb ore in white clays is responsible for high Zn and Pb
245 grade (up to 320000 ppm for Zn and 37100 ppm for Pb).

246 In ochre clayey material, clay minerals, quartz, calcite and dolomite are always present, with a
247 common occurrence of cerussite. Chemical compositions of the ochre and white clayey materials are
248 relatively close; indeed they have similar MgO and CaO contents (**Table 1**). Despite the absence of Zn-
249 bearing phases (sulphide or carbonate) detected from whole-rock XRD analysis, the Zn content varies
250 between 6275 ppm and 237000 ppm. 

251

252 The extreme variations of the Zn content in the three types of clayey material cannot be
253 correlated straightforwardly to the mineralogical composition deduced from whole rock XRD
254 measurement, it may be partly due to the presence of willemite impurities, but, for several samples
255 (ochre clays), Zn-bearing clays must be involved to explain tremendous Zn contents, requiring a
256 specific study of the clay fraction.

257

258 *4.2) Mineralogical characterisation of the clay fraction*

259

260 *4.2.1) Red clays*

261 XRD patterns obtained on the clay fraction of the red clays show a non-expandable phase
262 around 7.1 Å (**Fig. 4A**), which mainly corresponds to the 001 reflexion of kaolinite as this Bragg peak
263 disappears after heating to 550 °C. Chlorite is significantly present in the mixture as evidenced by the
264 003 peak at 4.74 Å, and the slight offset of 004 reflection (3.55 Å) relative to the 002 peak of kaolinite
265 (3.58 Å). The non-expandable peak at 10 Å may suggest the presence of illite, whereas the 14.6 Å peak
266 that expands to 16.8 Å for EG-treated preparations corresponds to swelling smectite. The broad shape
267 in the domain between smectite and illite 001 reflections suggests the presence of interstratified
268 illite/smectite. By focusing on the position of the 060 reflection (**Fig. 4B**), a main broad peak at 1.49-

269 1.50 Å is consistent with the predominance of dioctahedral species like kaolinite and illite, whilst the
270 secondary peak at 1.541-1.543 Å corresponds to a trioctahedral type like chlorite. Quartz and goethite
271 are also present.

272

273 4.2.2) White clays

274 XRD patterns of white clays display two identified Bragg peaks at 7.25 Å and 3.61 Å that
275 expand to 7.39 Å and 3.53 Å, respectively, for samples treated with EG (**Fig. 5A**). This indicates the
276 presence of randomly interstratified smectite and of another clay mineral, characterized at 7 Å such as
277 kaolinite or serpentine. This mixed-layered (ML) clay mineral, dominated by the 7 Å phase, coexists
278 with illite and occasional chlorite. Smectite was detected in samples BA130F and BA134F. Associated
279 phases such as cerussite, willemite, ~~goethite~~ and goethite commonly occur. Whilst the broad peak
280 around 1.50 Å, typical of dioctahedral clays corresponds to the position of 060 reflexion of illite, the
281 thin well-defined peak at 1.54 Å suggests a significant proportion of trioctahedral type clay minerals
282 (**Fig. 5B**). Although this may be confused with the 1.541 Å peak due to the 211 reflection of quartz, the
283 060 reflexion patterns are similar between samples which may (e.g. sample BA130F) or may not (e.g.
284 sample BA124F) contain quartz (**Fig. 5A**). For sample BA124, the offset of the broad peak to 1.51 Å is
285 probably an artefact due to a parasite reflexion of zinc silicate (e.g. 11 $\bar{6}$ for willemite or 530 for
286 hemimorphite).

287

288 4.2.3) Ochre clays

289 XRD patterns of the ochre clays do not strongly differ to those of the white clays, with the
290 presence of randomly interstratified smectite and 7 Å mineral (**Fig. 6A**). But the shift of this Bragg
291 peak to lower angular value after EG treatment (up to 7.72 Å and 3.45 Å) suggests a higher smectite
292 proportion in the ML. In addition, illite and smectite are also displayed, as well as cerussite and
293 goethite. The predominance of the trioctahedral type over the dioctahedral type is obviously shown on
294 the 060 reflexion pattern (**Fig. 6B**), with a well-defined thin peak around 1.542 Å and a broad and
295 unclear peak around 1.51 Å, probably polluted by the reflection of minor zinc minerals.

296

297 4.3) Cation-exchange capacity (CEC) of the different types of clays

298

299 Although previous observations obtained through XRD measurements have stressed out a
300 possible trend between the type of clays and the amount of Zn content, it does not provide any
301 information on the localization of Zn within the phyllosilicate structure (i.e. in the interlayer space as
302 an exchangeable cations or included in the phyllosilicate sheets). The CEC measurements represent an
303 easy and convenient method allowing one to determine the proportion of exchangeable zinc in the three
304 kinds of clay samples (**Table 2**). The CEC value of the red clays is between 30 and 38 meq/100g,
305 consistent with a mixture of illite, kaolinite and smectite. For 3 out of 4 samples, the amount of
306 exchangeable Zn represents less than 1% of the CEC and is therefore not significant. In contrast, for
307 sample BA121, which may be considered as an exception, more than 40% of the CEC contains
308 exchangeable Zn; this may partly explain the high Zn content (30000 ppm) of this sample, but this
309 assumption is not valid for other mineralized samples such as BA127 (**Table 1**). For the white clays,
310 the CEC values are bracketed between 9 and 27 meq/100g; it may be related to the high content of ML
311 dominated by a non-swelling 7 Å mineral, with a typical CEC value of 5 to 15 meq/100g (**Ma and**
312 **Eggleton 1999**). In the ochre clays, the CEC values may reach 41 meq/100g, as the smectite proportion
313 in the ML is probably higher than in the white clays (**Fig. 6A**). The amount of exchangeable zinc in the
314 CEC is very low for both white and ochre clays, suggesting that zinc is mainly included within the
315 octahedral sites of the clay mineral structure.

316

317 *4.4) Textural observations (OM and SEM)*

318

319 SEM observations of the red clays confirm the presence of a mixture of clay minerals, with
320 dense aggregates of clay platelets (**Fig. 4C**). EDS analyses show that clay minerals are composed of Si,
321 Al, and K, in accordance with the occurrence of illite/kaolinite mixture as identified on XRD patterns
322 (**Fig. 4A**). Isolated laths or sub-euhedral lamella of chlorite are associated to K-rich clays and quartz
323 sub-rounded clasts too (**Fig. 4C**). The bulk clayey matrix displays lighter and porous aggregates of
324 lamella-shaped minerals (**Fig. 4D**); EDS analyses of these patches show Zn enrichment and a low K
325 content relative to the mixture of kaolinite and illite. Descloizite, a zinc vanadate that precipitates under
326 high oxidizing weathering conditions has been locally found (**Fig. 4E**) and may explain, together with
327 the zinc clays, the anomalous high Zn content of some red clayey material samples (e.g. BA121 and

328 BA127; **Table 1**). It is worth to notice that no particular phase corresponding to zinc clays was detected
329 by XRD analyses suggesting a low abundance of these zinc-bearing minerals.

330 Optical microscope observations of the white clays show that clay minerals occur in cavity
331 within the ore formed by roundish aggregates of willemite and disseminated galena coated by cerussite
332 (**Fig. 5C**). SEM imaging of the clayey material in these cavities reveals a roughly honeycomb texture
333 of the newly formed clay minerals (**Fig. 5D**). Locally, the micrometre-sized clay sheets are densely
334 aggregated and form patches disseminated in the cavity. EDS analyses reveal that these clays are rich
335 in Zn and poor in K, but sometimes K-rich fragments are found, suggesting an intricate association of
336 both clay types. In most cases, the electronic contrasts between dark K-rich clays and light Zn-rich
337 clays are so clear that it is easy to separate to the related domains, which present a very different
338 textural arrangement (**Fig. 5E**). In the K-rich zone, the illite lamellae coexist with sub-euhedral clasts
339 of quartz. Thin to large bands of Zn-rich clays exposing a honeycomb texture pervade in the cavity and
340 connect to the willemite crystals.

341 Comparable observations can be made in the ochre clayey material, which exposes cavities
342 filled by clay minerals within a primary association of willemite, dolomite and cerussite (**Fig. 6C**). A
343 honeycomb texture of Zn-rich clays analysed by EDS is frequently observed (**Fig. 6D**). In the weakly
344 dense aggregates, the micrometre-sized clay crystals can be individualised, exposing a typical sheeted
345 aspect. Relics of illite lamellae and clasts made of quartz are found isolated in the Zn-rich clay matrix
346 (**Fig. 6E**).

347 The clay minerals and especially the zinc-bearing type are closely associated to willemite;
348 euhedral willemite crystals present evidence of partial dissolution that preferably affects edges or sites
349 of crystalline defect (**Fig. 7A**). Zinc clays may precipitate in this newly formed porosity (**Fig. 7B**), but
350 are mainly found as flakes or platelets either within the K-rich clayey material composed by illite,
351 kaolinite and chlorite (**Fig. 7C**) or along cleavage cracks to form mineralized ribbons (**Fig. 7D**) that
352 fossilized the paths of reactive waters. The honeycomb texture of newly formed zinc clays is frequent
353 in the core of the domain, whereas the clay sheets appear squeezed at the interface with willemite
354 (**Figs. 5E and 7E**). Together with the euhedral shape of the willemite crystal and the evidence of
355 successive rims of willemite, this supports the crystallization of a second generation of willemite
356 (willemite II in **Fig. 7F**) after the formation of the Zn-rich clays.

357

358 *4.4) Microprobe analyses of clay minerals*

359

360 WDS quantitative measurements have been carried out on clay aggregates from white and
361 ochre types (samples BA02, BA05 and BA05) and the results are reported in **Table 3**. Only data with a
362 total over 80 %wt, consistent with the range of expected zinc clays minerals (fraisontite, sauconite)
363 have been retained for discussion. The ZnO content, between 1.86 % and 49.39 % appears negatively
364 correlated to the K₂O content varying from 10.01 % to 0.05 %. Similarly, the SiO₂ and Al₂O₃ contents
365 decrease with K₂O. Ca, Fe, Mg and Pb cations are present in minor amount and we observe ~~show~~ slight
366 variations without any relationships with other major elements. Several groups depending on their ZnO
367 and K₂O content and their total oxide content have been distinguished (**Table 3**).

368 For K-rich clayey material, structural formulae were calculated for 22 negative charges (**Table**
369 **3**). For analyses 10, 57 and 58, the number of octahedral cations is around 2 and the number of
370 interlayered cations reaches 0.8, consistent with the occurrence of illite. Analyses 19, 20, 29 and 38
371 show a significant K₂O content (around 2 %) and Zn enrichment up to 30 %; they present a total of
372 analysed oxides around 84 % consistent with pure Zn smectite, i.e. sauconite (**Table 3**). For seven
373 individuals analyses that present a total of analysed oxides around 93 % and a K₂O content between 0.2
374 % and 0.6 %, structural formulae were calculated for 22 negative charges assuming a T-O clay mineral
375 structure. The number of cations in octahedral sites is around 5.5 attesting that the analysed particles
376 are trioctahedral Zn-rich T-O minerals such as fraipontite. The value of M⁺ (M⁺=K+2Ca) is
377 significantly high, and may mirror surface adsorption of alkaline cations. The 17 remaining analyses
378 display a total oxide between 84 % and 93 % and/or a variable content in K₂O; they probably
379 correspond to a mixture of the above-mentioned end-member clay minerals. The structural formulae
380 calculations were based on 22 negative charges. One can notice the number of cations in the octahedral
381 sites (3.4-3.5) largely exceed the ideal value of 3 (**Table 3**).

382

383 **5) Discussion**

384

385 *5.1) Identification of the nature of Zn clays*

386

387 The results obtained from microscopic observation and XRD analysis, suggest the presence of
388 Zn-bearing clays in the three types of clayey material at Bou Arhous mine, especially in the white and
389 ochre types. By comparing the results given by the two methods, we can deduce that the zinc-rich
390 sheeted aggregates disseminated in the samples correspond to a 7 Å mineral locally interstratified with
391 smectite sheets. In the literature, several types of zinc clays have been described. Sauconite, a
392 trioctahedral smectite close to saponite is the most described clay type and was reported in several
393 deposits in Northern America (**Ross 1946**), Peru (**Boni et al. 2009a**), Southern Africa (**Kärner 2006**;
394 **Terraçiano 2008**; **Boni et al. 2011**) and Iran (**Daliran et al. 2009**). Fraipontite (also known as
395 zinalcite), a zincian berthierine (7 Å mineral) has been found in supergene zinc deposits in Belgium
396 (**Fransolet and Bourguignon 1975**), Iberia (**Calvo et al. 2007**; **Will et al. 2014**), Italy (**Merlino and**
397 **Orlandi 2001**) and Kazakhstan (**Chukhrov 1968**). Other rare zinc clays are Zn-rich beidellite
398 (**Mondillo et al. 2014**), baileychlore, a zinc chlorite (**Rule and Radke 1988**) and hendricksite, a zinc
399 mica (**Fron del and Ito 1966**; **Robert and Gaspérin 1985**), the latter two occurring in hypogene
400 environments. Besides, moresnetite (**Ross 1946**) and vanuxemite (**Fron del 1972**) have been described
401 as a mixture of zinciferous clays and hemimorphite. No zinc-bearing mixed-layered (ML) minerals
402 have been described, except for illite-zincian smectite ML in Peru (**Mondillo et al. 2014**).

403 In this study, the WDS compositions of the clay crystals show a negative correlation between
404 K (as well as Al and Si) and Zn, suggesting phase mixing at site of analysis (**Table 3**). This is in
405 agreement with the microscopic observation that supports an intricate association between the K-rich
406 and the Zn-rich clays. In the $M^{+} - 4Si - 3R^{2+}$ ternary plot, classically used for distinguishing the
407 dioctahedral and the trioctahedral types (**Meunier 2005**), our data are scattered along a mixing line that
408 joins the mica pole and the most frequent Zn-clays, namely sauconite and fraipontite (**Fig. 8**). The data
409 corresponding to the purest Zn-clays do not fall into fields of natural sauconite or fraipontite collected
410 in Peru (**Boni et al. 2009a**; **2009b**), in Namibia (**Kärner et al. 2006**), in the USA (**Ross 1946**), in UK
411 (**Young et al. 1992**) and in Belgium (**Fransolet and Bourguignon 1975**); data rather fall into an
412 intermediate domain between the theoretical compositions of sauconite and fraipontite. Together with
413 the difficulty of calculating pure sauconite or fraipontite structural formula from our analyses (**Table**
414 **3**), this indicates that our zinc clayey material is dominantly a mixture of fraipontite and sauconite, in
415 agreement with the occurrence of interstratified smectite and 7 Å mineral.


416 Numerical modelling of XRD patterns using the Newmod © program (**Reynolds 1985**) have
417 been carried out to determine the relative proportions of fraipontite and sauconite in the ML mineral.
418 Assuming 1) a mixture of a two-water-layer tri-smectite and a 7 Å mineral, 2) the 00l reflexions given
419 by Faust (**1951**) and Franolet and Bourguignon (**1975**), and 3) a Reichweite value of 0, we have
420 produced the XRD patterns presented in **Figure 9**. In this calculation, we have neglected the minor
421 effects of Zn²⁺ on the geometry of ML structure and therefore on the theoretical positions of 00l
422 reflexions. The best simulation to describe the measured XRD pattern is obtained for a mixture
423 containing 80% of fraipontite and 20% of sauconite, namely R0 fraipontite (0.8)/sauconite (**Fig. 9**). To
424 validate this composition, we have recalculated the structural formula assuming a mixing of sauconite
425 and fraipontite at a ratio of 1:4. Based on 39O, the sum of cations in the octahedral sheets is between
426 14.2 and 15 for low K₂O individual data; this value, slightly lower than the ideal value of 15 for the
427 trioctahedral type corroborates the hypothesis of R0 fraipontite(0.8)/sauconite mixed-layered mineral
428 as the zinc-bearing clay mineral. Although such composition of interstratified mineral has never been
429 reported in the literature, the occurrence of the sauconite-fraipontite association has been described in
430 several natural examples of supergene non-sulphide zinc deposits (**Foord et al. 1983; Young et al.**
431 **1992; Maltsev and Korshunov 1988**), or even found in experimental works (**Esquivin 1957; 1960**).

432

433 *5.2) Genetic processes accounting for Zn-clays formation*

434

435 Results obtained on whole-rock samples show the difficulty of identifying significant differences
436 between the three types of clayey material to understand their genetic link with the ore and the host
437 rock. Despite these difficulties, the following implications may be deduced from the above-mentioned
438 analysis:

439 - Dolomite is present in the Jurassic limestone and in the gangue of Zn-Pb ore. Its occurrence
440 in the ochre and white clayey materials and its relative absence in the red one may indicate different
441 genetic processes accounting for their respective origin. 

442 - Microscope observations have shown that Zn-clays are very frequently associated to detrital
443 illite, which is dominant in the red clayey material. Zinc enrichment of clay minerals in the white and
444 ochre clayey materials is consistent with the neogenesis of mixed layered fraipontite(0.8)/sauconite
445 minerals, requiring sources for zinc, silica and aluminium.

446 - The main zinc-bearing mineral at Bou Arhous is willemite, whose conditions of formation
447 remain unclear (Choulet et al. 2014). It may have been formed under supergene conditions as
448 exemplified by the deposits in Nevada (Takahashi 1960), or in Zambia (Terraciano 2008).
449 Alternatively, a hydrothermal or hypogene origin for willemite (Brugger et al. 2003; Hitzmann et al.
450 2003, Boni et al. 2011) could be envisaged, but no field and mineralogical observations are currently
451 supporting this hypothesis.

452 The origin of willemite in such supergene environment is not clearly understood as this
453 mineral is mostly described in hypogene or hydrothermal deposits (Hitzman et al. 2003; Coppola et
454 al. 2008). Its occurrence at Bou Arhous may suggest either a low-temperature hydrothermal stage or
455 exceptional physico-chemical conditions characterised by a combination of high silica activity, low
456 $P(\text{CO}_2)_g$, alkaline conditions and oxidizing environment (Choulet et al. 2014). At 25°C, willemite may
457 be partly dissolved by meteoric waters rich in Ca and poor in Si (Brugger et al. 2003); such conditions
458 are reached in karst environment because of water-host rock interaction. This can explain the evidence
459 for supergene dissolution of willemite, releasing Zn and Si in the solution (Figs. 7A and 7B). This
460 dissolution is probably congruent as no quartz or silica gel, incorporating the silicon in excess, remains
461 or precipitates in the secondary porosity. The addition of Zn and Si ions in the solution changes
462 equilibrium and the solubility of the Zn-bearing phases strongly depends on the pH conditions
463 (Takahashi 1960; Brugger et al. 2003). As no smithsonite or hydrozincite precipitation has been
464 observed in our samples despite high $P(\text{CO}_2)_g$ due to karst buffering, slightly acid (ca. 5) conditions
465 must be envisaged to transport the Zn^{2+} ions as chlorozinc(II) complexes (Ruaya and Seward 1986)
466 and to enable a further precipitation of zinc clays. The absence of widespread hemimorphite is difficult
467 to understand, as this phase is supposed to precipitate under acid pH conditions and relatively high
468 silica activity (Takahashi 1960; McPhail et al. 2003); however, this may be explained by the limited
469 field of hemimorphite stability and its sensibility to strong $P(\text{CO}_2)_g$ variations (Reichert and Borg
470 2008).

471 The availability of Al is also critical for the neogenesis of the Zn clays, and requires a local
472 source because of the low mobility of Al in meteoric waters. The Zn clays are often associated to the
473 K-rich clays, mainly illite as evidenced by the XRD patterns of the white and ochre clayey materials.
474 At the scale of the cavity, the pervasion of the Zn-rich clays in the material dominated by the K-rich
475 clays shall suggest a pseudomorphosis of primary illite and smectite and their replacement by the

476 mixed-layered clay minerals (**Figs. 5D or 6E**). The very close association of illite and Zn clays
477 suggests that partial dissolution of external illite layers, due to hydrolysis and the break up of Al-O and
478 Si-O bonds, contributes to releasing Al and Si, further incorporated in the newly formed ML clay
479 minerals. The Zn clays may also pseudomorph after dissolved willemite (**Fig. 7B**), but this requires a
480 close source for Al.

481 In karstic environments, the physico-chemical conditions of meteoric waters continuously
482 change due to carbonate buffering. A rapid increase of pH causes tremendous variations of the
483 solubility of zinc silicates like willemite that can further precipitate even at surface temperature and
484 under neutral conditions (**Brugger et al. 2003**). This precipitation of secondary willemite (Willemite
485 II) forming euhedral rim around primary willemite (willemite I) leads to squeezing of newly formed
486 zinc clays (**Fig. 7E and 7F**). As a consequence, the honeycomb texture is locally erased, and jamming
487 contributes to emphasize the very fine mixing between illite and ML clay minerals (**Fig. 7E**).
488 Secondary willemite also occurs as idiomorphic crystals in the open space of the clayey cavities (**Fig.**
489 **7D**) or as infilling material within fractures of primary willemite (**Fig. 7F**).

490

491 *5.3) Conditions for Zn mineralisation of clays and relation to the ore evolution*

492

493 The mechanisms of Zn-rich clays formation have been rarely reported in the literature. In Zn
494 ore deposits of Peru, Boni et al. (**2009a**) have identified sauconite and altered feldspars and they
495 proposed that sauconite in silicoclastic host rocks may result from interaction between feldspar
496 weathering and Zn-rich solution derived from supergene dissolution of zinc sulphide. At Abenab West
497 ore deposit (Namibia), hosted in limestone, a progressive enrichment in Zn and Mg of barren clays is
498 suggested, but details of the nature of zinc clays and the processes related to their neogenesis are
499 presently not available (**Terraciano 2008**).

500

501 Like Abenab West ore deposit, zinc ore at Bou Arhous is hosted in limestone that has
502 developed a large karst network since its exhumation at surface (**Leblanc 1968**). The Bou Arhous karst
503 presents some non-dissolved material concentrated in various-sized cavities. Field observations have
504 shown that this red clayey material is composed by a fine succession of silt and clay horizons that
505 present sedimentation features. The red clay type may correspond to "residual" clays, which generally
show mixing components between detrital sources and insoluble parts of the dissolved limestone

506 (Chamley 1989). The residual red clays are composed of clay minerals like illite, chlorite, kaolinite
507 and smectite, iron oxi-hydroxide and quartz. This composition is somehow similar to that of the
508 classical peri-Mediterranean karst-related clayey infilling, known as *terra rossa*, that shows stratiform
509 accumulation of red clayey material in cavity formed after limestone dissolution (e.g. Blanc and
510 Chamley 1975; Moresi and Mongelli 1988; Iacoviello and Martini 2013).

511 The red clays are originally barren (Table 1), but may be fertilized by several complementary
512 processes that includes:

- 513 - Sedimentary recycling of zinc ore fragments, such as willemite (Figs. 3C and 3D).
- 514 - Precipitation of newly formed zinc-bearing minerals like descloizite (Fig. 4E), which is
515 typical of high oxidising supergene environment (Boni et al. 2007).
- 516 - Adsorption of the Zn^{2+} cations at the clay surface or fixing of the Zn^{2+} cations in the
517 interlayer, as indicated by the amount of $[Zn^{2+}]$ released after the CEC measurements (Table 2). This
518 process is well known in the literature as many studies have focused on the capacity of clays to trap
519 heavy metals like Zn (e.g. Bradbury and Baeyens 1999; Dähn et al. 2011).
- 520 - Precipitation of the Zn-rich clays in small-disseminated patches (Fig. 4D), up to large
521 pervasion (Figs. 5D and 6E) in the red detrital clayey material. This process is able to progressively
522 form the white or the ochre clays found in the Bou Arhous deposit. As seen earlier, this process is
523 characterized by the neogenesis of authigenic clay minerals that nucleate on micas. It may be compared
524 to the epitaxial growth of Zn clays on smectites, which interacts with a solution enriched in Zn and Si
525 (Schlegel et al. 2001; Schlegel and Manceau 2006). These authors reported newly formed clays as a
526 mixture of Zn-saturated TO and TOT trioctahedral phyllosilicates, thereby presenting lot of similarities
527 with the R0 fraipontite(0.8)/sauconite mixed-layered mineral identified in this study. The presence of a
528 clay precursor for nucleation and Al supply is required for the neogenesis of Zn-clays, which also
529 depends on the silica activity (Schlegel et al. 2001). At low Si concentration, Zn may be fixed in
530 polymer chains in structural continuity to the smectite. High Si concentration rather facilitates the
531 neogenesis of authigenic clays and especially the formation of Zn-rich TO phyllosilicates, such as
532 fraipontite. Other experimental studies at supergene conditions have showed that the presence of Al
533 may play a role for the type of clay that precipitates (Tiller and Pickering 1974), with 2:1 layer
534 silicate in Al-free conditions and, in the presence of aluminium, formation of 1:1 layer silicate similar
535 to Zn berthierine, a synthetic product equivalent to fraipontite (Esquevin 1960). Such chemical

536 controls could be hypothesised to spell out the different types of Zn clays met throughout the world.
537 The climate dependence classically evoked for the variability of clay types (**Chamley 1989**) may also
538 be taken into account, but its role is currently difficult to understand, given the scarcity of reliable data
539 on Zn clay occurrences.

540 The formation of zinc clays at Bou Arhous is a continuous process during the late supergene
541 evolution of the ore deposit. Initially, zinc was included in sulphide lenses hosted in the Lower Jurassic
542 limestone (**Leblanc 1968**). The regional uplift and the folding episode related to the Atlas tectonics
543 during the Tertiary have led to an exhumation of the sulphide ore and a verticalisation of the limestone
544 strata (**Choulet et al. 2014**). As a consequence, the meteoric water has percolated in the fractures and
545 has provoked the dissolution of the limestone and the oxidation of the sulphides. For some unclear
546 reasons, zinc has first re-precipitated as willemite, forming a “black ore” due to its association with
547 preserved galena and cerussite. Willemite has further interacted with karstic waters, probably poor in Si
548 and slightly acid, leading to its partial dissolution and to releasing of Zn and Si in the solution (**Fig.**
549 **10**). In parallel, the development of a karst was characterised by the opening of various-sized
550 dissolution cavities filled by detrital supplies and insoluble materials (**Fig. 10**). At surface conditions,
551 this red clayey material has been pervaded by Zn-Si-rich solutions resulting in the neogenesis of Zn-
552 clays (mixed-layered clay minerals) that nucleate on detrital micas. At site of zinc ore concentration,
553 red clays were progressively transformed into white and ocher clays. The further crystallisation of late
554 generations of willemite indicates that this process is continuous in time, highly dependant on the
555 chemistry and dynamics of karstic solutions, and therefore difficult to timely constrain in the ore
556 deposit evolution.

557

558 **6) Conclusion**

559

560 This study has revealed the nature of the zinc clays at Bou Arhous deposit and the
561 mechanisms called for their genesis. Although several processes are involved for the metal enrichment
562 of barren clays, the crystallisation of Zn clays appears to be the major one. This neogenesis is related to
563 the interaction between Zn-rich meteoric water and residual clays related to karst evolution. This model
564 has strong implication for the mineral industry, as Zn-rich clayey material grading up to 30% Zn is a
565 non-negligible resource that may be easily identified. The target zones will be the karst cavities located

566 around the original ore body (potentially dissolved); residual clays must fill these cavities, representing
567 the necessary condition for the nucleation of the newly formed clay crystals. The soft nature of the
568 clayey material could probably facilitate mining, at least in case of open-pit extraction, and especially
569 contributes to costs reduction in the early operations.

570 Conversely, by deciphering the mineralogical nature of the Zn-rich clayey material, this study
571 has showed the mixture of authigenic mixed-layered clays and detrital phyllosilicates. Except for rare
572 samples, zinc cannot be recovered easily as it is located within the octahedral sites in each component
573 of the interstratified mineral. Consequently, Zn can only be released by leaching techniques such as
574 solvent extraction, which is relatively efficient for a given clay species like sauconite (**Boni et al.**
575 **2009b**). But, in the presence of interstratified minerals finely disseminated within detrital barren clays,
576 ore liberation may be more difficult and requires advances for 1) an efficient separation between barren
577 and mineralised clays, and 2) a better selectivity of solvents used. Another consequence of this intricate
578 mineralogical association is the excess of barren materials that need to be handled and processed,
579 thereby representing a major limitation to the economic potential of zinc clays.

580

581 **Acknowledgments**

582

583 The authors are indebted to Managem Company for providing access to the Bou Arhous Mine and for
584 having supported bulk rock analyses in their labs. We also thank Goka Katrawi for CEC measurements
585 and Didier Convert-Gaubier for thin-section preparation. This study has benefited from a research grant
586 given by the Région Centre for the 2011-2014 CALAMINES project and from a financial support of
587 Région Franche-Comté with the 2014 “Franco-Suisse” call. Access to SEM facilities of the
588 MIMENTO centre was made in the frame of cooperative projects in the Renatech network.

589

590 **Figure Captions**

591

592 **Fig. 1** a: Simplified tectonic map of Morocco. b: Geological map of the Bou Arhous range. c: Cross-
593 Section across the Bou Arhous range, showing the structural and stratigraphic location of the ore
594 deposit (modified after **Choulet et al. 2014**)

595

596 **Fig. 2** a: Non-sulphide ore veins cropping out at the surface. b: Lower Jurassic host rock composed of
597 limestone and marl strata. c: Triassic variegated shale inside the mine. d: Preserved sulphide associated
598 to calcite and willemite in a “black ore” vein. e: Illustration of the different types of clayey material
599 with relationships to “black ore”

600

601 **Fig. 3** a: Association of red clays and white to ochre clays inside the mine. b and c: Details of the
602 interconnected karst cavities, filled by red clayey material showing shallow inclined bedding. d: White
603 clays at the interface between the black ore and the red clays. e: Large occurrence of white clays
604 around black ore. f: Cavity filled by ochre clays spotted by relics of black ore

605

606 **Fig. 4** a: XRD patterns of representative samples of red clayey material (oriented clay fraction
607 preparation). See text for details about Bragg peaks indexation. Black (red) curves were obtained in dry
608 (Ethylene glycol (EG)) conditions. Sm: smectite, K: kaolinite, Ill: illite, Chl: chlorite, Qz: quartz, Goe:
609 goethite. b: XRD patterns (misoriented clay fraction preparation) emphasizing the position of 060
610 reflections for representative samples of red clayey material. c to e: BSE images of red clays
611 illustrating the detrital origin of this material that contains a mixture of chlorite, illite, smectite, quartz
612 clasts and secondary Zn-rich mineral patches

613

614 **Fig. 5** a: XRD patterns of representative samples of white clayey material (oriented clay fraction
615 preparation) Sm: smectite, Ill: illite, ML: mixed-layers, Will: willemite, Cc: cerusite, Qz: quartz. b:
616 XRD patterns (misoriented clay fraction preparation) emphasizing the position of 060 reflections for
617 representative samples of white clayey material. c: Illustration of cavities filled with white clays inside
618 the black ore (transmitted light, crossed nichols). d: BSE image of the mixture of Zn-rich clays and K-
619 rich clays, with light grey patches composed by Zn-rich clays. e: BSE image of zinc clays aggregate in
620 cavities filled by detrital clays and relationships between clays and willemite crystals

621

622 **Fig. 6** a: XRD patterns of representative samples of ochre clayey material (oriented clay fraction
623 preparation) Sm: smectite, Ill: illite, ML: mixed-layers, Will: willemite, Qz: quartz; b: XRD patterns
624 (misoriented clay fraction preparation) emphasizing the position of 060 reflections for representative
625 samples of ochre clayey material. c to e: BSE images of the ochre clayey material. c: relationships

626 between zinc clays and ore and gangue minerals (willemite, cerussite and dolomite). d and e: Detailed
627 view of the zinc clays, with disseminated relics of detrital micas and quartz

628

629 **Fig. 7** Secondary (a and f) and back-scattered (b to e) electron images of willemite and zinc clays in
630 black ore and white to ochre clay samples. a: partially dissolved willemite crystal with clay particles on
631 its surface. b: Neogenesis of authigenic zinc clays that precipitate in the void created by the partial
632 dissolution of a willemite crystal. c: Newly formed zinc clays flakes precipitating on detrital micas
633 surfaces. d: Ribbon-like aggregates of zinc clays filling the space between detrital clays. Note the
634 precipitation of late euhedral willemite crystals (willemite II) in the porosity. e: Pervasive enrichment
635 in zinc clays of a geode initially filled by detrital clays. Note the idiomorphic willemite crystals close to
636 squeezed zinc clays; this crushed texture suggests willemite growth after zinc clays formation. f:
637 Polyphase crystallization of willemite, showing growth zoning and fracture infilling

638

639 **Fig. 8** $4Si-M^{+}-3R^{2+}$ diagram, illustrating the mixture of di- and tri-octahedral end-members. Our data
640 are plotted as square symbols and are compared with data reported in the literature. Colour assignment
641 matches the different types as showed in Table 3. Red: mica, green: fraipontite, blue: sauconite and
642 black: mixture of these three end-members

643

644 **Fig. 9** Calculated XRD patterns given by Newmod modelling. Black (red) curves were obtained in dry
645 (Ethylene glycol (EG)) conditions. See text for data inputs and implications

646

647 **Fig. 10** Schematic view illustrating the formation of zinc clays in a mineralised karstic environment.
648 The relationships between the black ore (supergene non-sulphide ore) and the residual clays are
649 emphasized. The two BSE images show the detrital texture of red clays before zinc mineralisation
650 (right) and the honeycomb texture of white to ochre clays after neogenesis of zinc clays (left)

651

652 **Table 1** Sampling details of the host rocks and clayey material, with bulk mineralogy deduced from
653 XRD and geochemical content obtained by ICPMS analyses. Abbreviations: cc: calcite, ce: cerussite,
654 cl: clays, do: dolomite, ga: galena, goe: goethite, gy: gypsum, he: hematite, qtz: quartz

655

656 **Table 2** Values of the CEC and zinc content of the CEC for the three types of clay materials reported
657 in this study. The clay content is deduced from XRD analyses and is illustrated in figs 4 to 6

658

659 **Table 3** WDS results and calculated structural formulae for the different types of clay minerals and
660 aggregates. See text for explanation about calculation and data sorting

661

662 **References**

663

664 Abkhoshk E, Jorjani E, Al-Harashsheh MS, et al (2014) Review of the hydrometallurgical processing of
665 non-sulfide zinc ores. *Hydrometallurgy* 149:153–167. doi: 10.1016/j.hydromet.2014.08.001

666 Ammann L, Bergaya F, Lagaly G (2005) Determination of the cation exchange capacity of clays with
667 copper complexes revisited. *Clay Minerals* 40:441–453. doi: 10.1180/0009855054040182

668 Bayraktar I, Aslan A, Ersayin S (1998) Effects of primary slime and clay on selectivity of flotation of
669 sub-volcanogenic complex polymetallic ores. *Trans Instit Min Metal Sect B Applied Earth Sci*
670 107:C71–C76

671 Blanc J, Chamley H (1975) Remplissages de réseaux karstiques à la grotte de Saint-Marcel d’Ardèche.
672 *Quaternary* 12:71–82. doi: 10.3406/quate.1975.2084 (in French)

673 Boni M, Large D (2003) Nonsulfide Zinc Mineralization in Europe: An Overview. *Econ Geol* 98:715–
674 729. doi: 10.2113/gsecongeo.98.4.715

675 Boni M, Terracciano R, Evans NJ, et al (2007) Genesis of Vanadium Ores in the Otavi Mountainland,
676 Namibia. *Econ Geol* 102:441–469. doi: 10.2113/gsecongeo.102.3.441

677 Boni M, Balassone G, Arseneau V, Schmidt P (2009a) The Nonsulfide Zinc Deposit at Accha
678 (Southern Peru): Geological and Mineralogical Characterization. *Econ Geol* 104:267–289. doi:
679 10.2113/gsecongeo.104.2.267

680 Boni M, Schmidt PR, De Wet JR, et al (2009b) Mineralogical signature of nonsulfide zinc ores at
681 Accha (Peru): A key for recovery. *Int J Mineral Processing* 93:267–277. doi:
682 10.1016/j.minpro.2009.10.003

683 Boni M, Terracciano R, Balassone G, et al (2011) The carbonate-hosted willemite prospects of the
684 Zambezi Metamorphic Belt (Zambia). *Miner Deposita* 46:707–729. doi: 10.1007/s00126-011-0338-

685



686 Bradbury MH, Baeyens B (1999) Modelling the sorption of Zn and Ni on Ca-montmorillonite. *Geoch*
687 *Cosmoch Acta* 63:325–336. doi: 10.1016/S0016-7037(98)00281-6

688 Brugger J, McPhail DC, Wallace M, Waters J (2003) Formation of Willemite in Hydrothermal
689 Environments. *Econ Geol* 98:819–835. doi: 10.2113/gsecongeo.98.4.819

690 Calvo M, Viñals J, Triviño A (2007) Zálesiíte, felsobanyaite and fraipontite, in a conglomerate in
691 Prullans, La Cerdanya, Catalonia (Spain). *Mineral Up* 1:49–51

692 Chamley H (1989) *Clay sedimentology*. Springer-Verlag, Berlin Heidelberg

693 Choulet F, Charles N, Barbanson L, et al (2014) Non-sulfide zinc deposits of the Moroccan High Atlas:
694 Multi-scale characterization and origin. *Ore Geol Rev* 56:115–140. doi:
695 10.1016/j.oregeorev.2013.08.015

696 Chukhrov FV (1968) Some Results of the Study of Clay Minerals in the U.S.S.R. *Clays and Clay*
697 *Minerals* 16:3–14. doi: 10.1346/CCMN.1968.0160103

698 Churakov SV, Dähn R (2012) Zinc Adsorption on Clays Inferred from Atomistic Simulations and
699 EXAFS Spectroscopy. *Environ Sci Technol* 46:5713–5719. doi: 10.1021/es204423k

700 Connelly (2011) High clay ores: a mineral processing nightmare part 2. *Australian J Mining* 4

701 Coppola V, Boni M, Gilg HA, et al (2008) The “calamine” nonsulfide Zn–Pb deposits of Belgium:
702 Petrographical, mineralogical and geochemical characterization. *Ore Geol Rev* 33:187–210. doi:
703 10.1016/j.oregeorev.2006.03.005

704 Crundwell F, Moats M, Ramachandran V, et al (2011) *Extractive Metallurgy of Nickel, Cobalt and*
705 *Platinum Group Metals*. Elsevier, Oxford

706 Dähn R, Baeyens B, Bradbury MH (2011) Investigation of the different binding edge sites for Zn on
707 montmorillonite using P-EXAFS – The strong/weak site concept in the 2SPNE SC/CE sorption
708 model. *Geoch Cosmoch Acta* 75:5154–5168. doi: 10.1016/j.gca.2011.06.025

709 Daliran F, Armstrong R, Borg G, et al (2009) Nonsulphide Zinc Deposits, Iran - The Hypogene
710 Emplacement and Supergene Modification History of the Angouran Zinc Deposit, NW-Iran.
711 *Bundesanstalt für Geowissenschaften und Rohstoffe*

712 De Wet JR, Singleton JD (2008) Development of a viable process for the recovery of zinc from oxide
713 ores. *J South Afr Instit Mining Metal* 108:253

714 Esquevin J (1957) Sur la composition minéralogique des moresnétites et l'existence probable d'une
715 nouvelle phyllite zincifère. Comptes Rendus de l'Académie des Sciences (Paris) A/3150:4022. (in
716 French)

717 Esquevin J (1960) Les Silicates de zinc, étude de produits de synthèse et des minéraux naturels. Institut
718 national de la recherche agronomique, Saint-Amand (in French)

719 Faust GT (1951) Thermal analysis and X-ray studies of sauconite and of some zinc minerals of the
720 same paragenetic association. *Am Mineral* 36:795–822

721 Foord EE, Taggart JE, Conklin NM (1983) Cuprian fraipontite and sauconite from the Defiance-Silver
722 Bill mines, Gleeson, Arizona. *Mineral Record* 14:131–132

723 Fransolet A-M, Bourguignon P (1975) Données nouvelles sur la fraipontite de Moresnet (Belgique).
724 *Bull Soc Fr Mineral* 98:235–244

725 Frizon de Lamotte D, Leturmy P, Missenard Y, et al (2009) Mesozoic and Cenozoic vertical
726 movements in the Atlas system (Algeria, Morocco, Tunisia): An overview. *Tectonophysics* 475:9–
727 28. doi: 10.1016/j.tecto.2008.10.024

728 Frondel C (1972) The minerals of Franklin and Sterling Hill, a checklist. Wiley-Interscience, New
729 York

730 Frondel C, Ito J (1966) Hendricksite, a new species of mica. *Am Mineral* 51:1107–1123

731 Fuerstenau MC, Jameson GJ, Yoon R-H (2007) Froth Flotation: A Century of Innovation. SME,
732 Englewood

733 Gauderoy C (1959) Kaolinite et montmorillonite zincifères (sauconite?) d'Iboughalène. *Not Mem du*
734 *Serv Geol Maroc* 144:152–153

735 Gnoinski J (2007) Skorpion Zinc: optimization and innovation. *J South Afr Instit Mining Metal*
736 107:657–662

737 Hitzman MW, Reynolds NA, Sangster DF, et al (2003) Classification, Genesis, and Exploration Guides
738 for Nonsulfide Zinc Deposits. *Econ Geol* 98:685–714. doi: 10.2113/gsecongeo.98.4.685

739 Iacoviello F, Martini I (2013) Clay minerals in cave sediments and terra rossa soils in the Montagnola
740 Senese karst massif (Italy). *Geol Quarterly* 57:527–536

741 Kärner K (2006) The metallogenesis of the Skorpion non-sulphide zinc deposit, Namibia. Dissertation,
742 Universität Martin Luther

743 Leblanc M (1968) Etude géologique et métallogénique du jbel Bou-Arhous et de son prolongement
744 oriental (Haut Atlas marocain oriental). Not Mem Serv geol Maroc 206:117–206 (in French)

745 Lim J (2011) Controlling clay behaviour in suspension: developing a new paradigm for the minerals
746 industry. Dissertation, University of Melbourne

747 Ma C, Eggleton RA (1999) Cation Exchange Capacity of Kaolinite. *Clays and Clay Minerals* 47:174–
748 180. doi: 10.1346/CCMN.1999.0470207

749 Maltsev V, Korshunov V (1998) Geochemistry of fluorite and related features of the Kugitangtou
750 Ridge Caves, Turkmenistan. *J Caves Karst Stud* 60:151–155

751 Mattauer M, Tapponnier P, Proust F (1977) Sur les mécanismes de formation des chaînes
752 intracontinentales; l'exemple des chaînes atlasiques du Maroc. *Bull Soc Geol fr S7-XIX*:521–526.
753 doi: 10.2113/gssgfbull.S7-XIX.3.521 (in French)

754 McPhail DC, Summerhayes E, Welch S, Brugger J (2003) The geochemistry and mobility of zinc in
755 the regolith. Cooperative Research Centre for Landscape Environments and Mineral Exploration
756 <http://crcleme.org.au/Pubs/Advancesinregolith/AdvancesinRegolith.html>.

757 Meier LP, Kahr G (1999) Determination of the Cation Exchange Capacity (CEC) of Clay Minerals
758 Using the Complexes of Copper(II) Ion with Triethylenetetramine and Tetraethylenepentamine.
759 *Clays and Clay Minerals* 47:386–388. doi: 10.1346/CCMN.1999.0470315

760 Merlino S, Orlandi P (2001) Carraraite and zaccagnaite, two new minerals from the Carrara marble
761 quarries: their chemical compositions, physical properties, and structural features. *Am Mineral*
762 86:1293–1301

763 Meunier A (2005) *Clays*. Springer Verlag, Berlin Heidelberg

764 Mondillo N, Nieto F, Balassone G, Boni M (2014) Zn-rich clay minerals in supergene ores (Cuzco
765 area, Peru); a TEM study with inferences for genesis and processing IMA meeting, Johannesburg.

766 Moresi M, Mongelli G (1988) Underlying limestones and dolostones in Apulia, Italy. *Clay Minerals*
767 23:439–446

768 Newman ACD (1987) *Chemistry of clays and clay minerals*. Wiley, New-York

769 Reichert J, Borg G (2008) Numerical simulation and a geochemical model of supergene carbonate-
770 hosted non-sulphide zinc deposits. *Ore Geol Rev* 33:134–151. doi:
771 10.1016/j.oregeorev.2007.02.006

772 Reynolds RCJ (1985) NEWMOD a computer program for the calculation of one-dimensional X-Ray
773 diffraction patterns of mixed-layered clays. Reynolds, R C J, 8 Brook Dr., Hanover, New
774 Hampshire

775 Robert J-L, Gasperin M (1985) Crystal structure refinement of hendricksite, a Zn- and Mn-rich
776 trioctahedral, potassium mica: a contribution to the crystal chemistry of zinc-bearing minerals.
777 *Tschermaks Minerale Petrograph Mitteil* 34:1–14

778 Ross CS (1946) Sauconite - a clay mineral of the montmorillonite group. *Amer. Miner.*, 31: 411. *Am*
779 *Mineral* 31:411–424

780 Ruaya JR, Seward TM (1986) The stability of chlorozinc(II) complexes in hydrothermal solutions up to
781 350°C. *Geoch Cosmoch Acta* 50:651–661. doi: 10.1016/0016-7037(86)90343-1

782 Rule AC, Radke F (1988) Baileychlore, the Zn end member of the trioctahedral chlorite series. *Am*
783 *Mineral* 73:135–139

784 Schlegel ML, Manceau A (2006) Evidence for the nucleation and epitaxial growth of Zn phyllosilicate
785 on montmorillonite. *Geoch Cosmoch Acta* 70:901–917. doi: 10.1016/j.gca.2005.10.021

786 Schlegel ML, Manceau A, Charlet L, et al (2001) Sorption of metal ions on clay minerals. III.
787 Nucleation and epitaxial growth of Zn phyllosilicate on the edges of hectorite. *Geoch Cosmoch*
788 *Acta* 65:4155–4170. doi: 10.1016/S0016-7037(01)00700-1

789 Takahashi T (1960) Supergene alteration of zinc and lead deposits in limestone. *Econ Geol* 55:1083–
790 1115. doi: 10.2113/gsecongeo.55.6.1083

791 Teixell A, Arboleya M-L, Julivert M, Charroud M (2003) Tectonic shortening and topography in the
792 central High Atlas (Morocco). *Tectonics* 22:1051. doi: 10.1029/2002TC001460

793 Terracciano R (2008) Willemite Mineralisation in Namibia and Zambia. Dissertation, Università degli
794 Studi di Napoli Federico II

795 Tiller KG, Pickering JG (1974) The Synthesis of Zinc Silicates at 20°C and Atmospheric Pressure.
796 *Clays and Clay Minerals* 22:409–416. doi: 10.1346/CCMN.1974.0220507

797 Warne JE (1988) Jurassic carbonate facies of the Central and Eastern High Atlas rift, Morocco. In:
798 Jacobshagen PDVH (ed) *The Atlas System of Morocco*. Springer Berlin Heidelberg, pp 169–199

799 Will P, Friedrich F, Hochleitner R, Gilg HA (2014) Fraipontite in the hydrothermally overprinted
800 oxidation zone of the Preguiça mine, Southern Portugal. Mid-European Clay Conference, Dresde.

- 801 Young B, Livingstone A, Thomson N (1992) Fraipontite from Wensleydale, North Yorkshire. Proc
802 Yorkshire Geol Soc 49:125–127. doi: 10.1144/pygs.49.2.125

Figure 2
Click here to download Figure: Fig2.tif

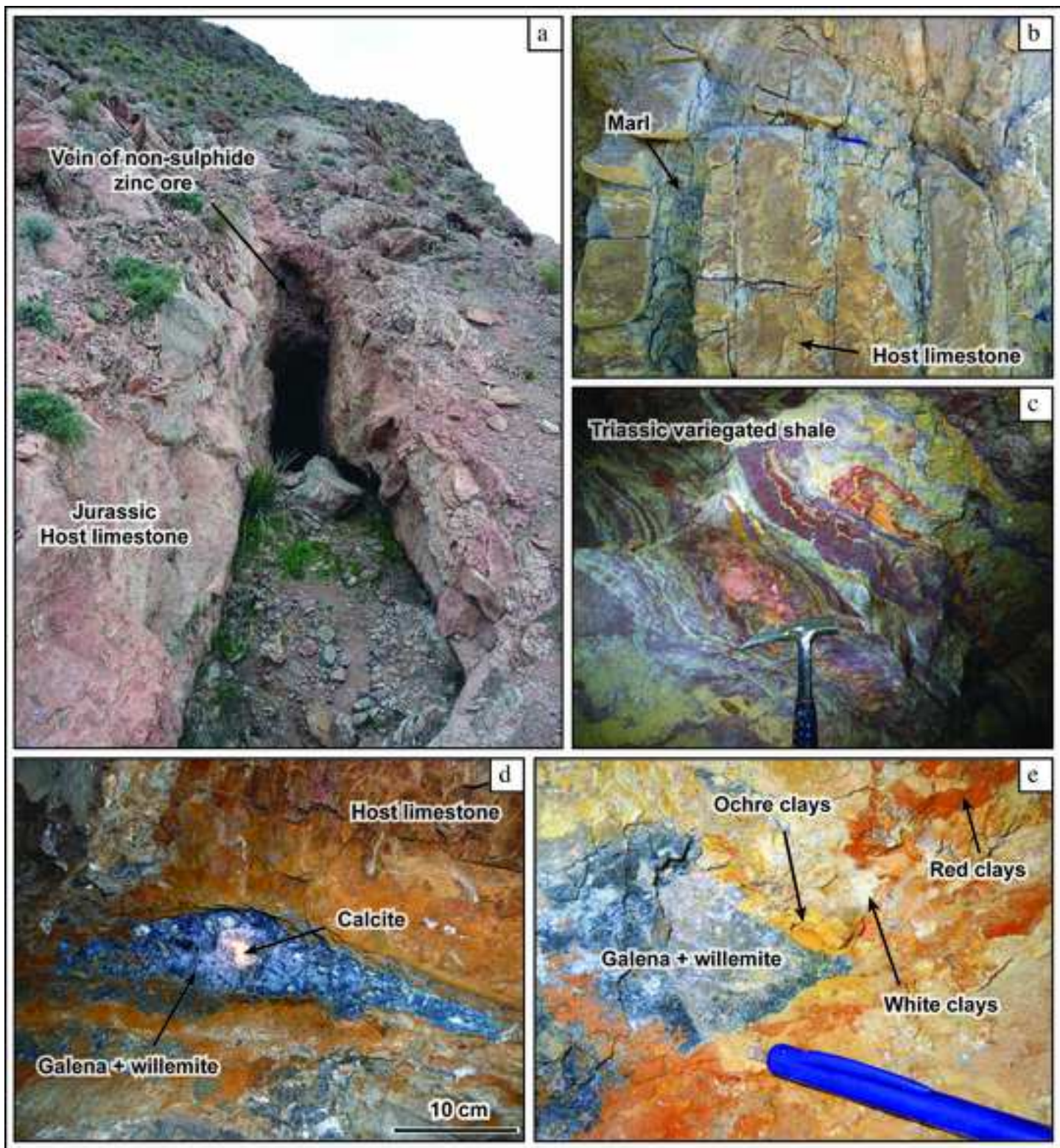


Figure 3
Click here to download Figure: Fig3.tif

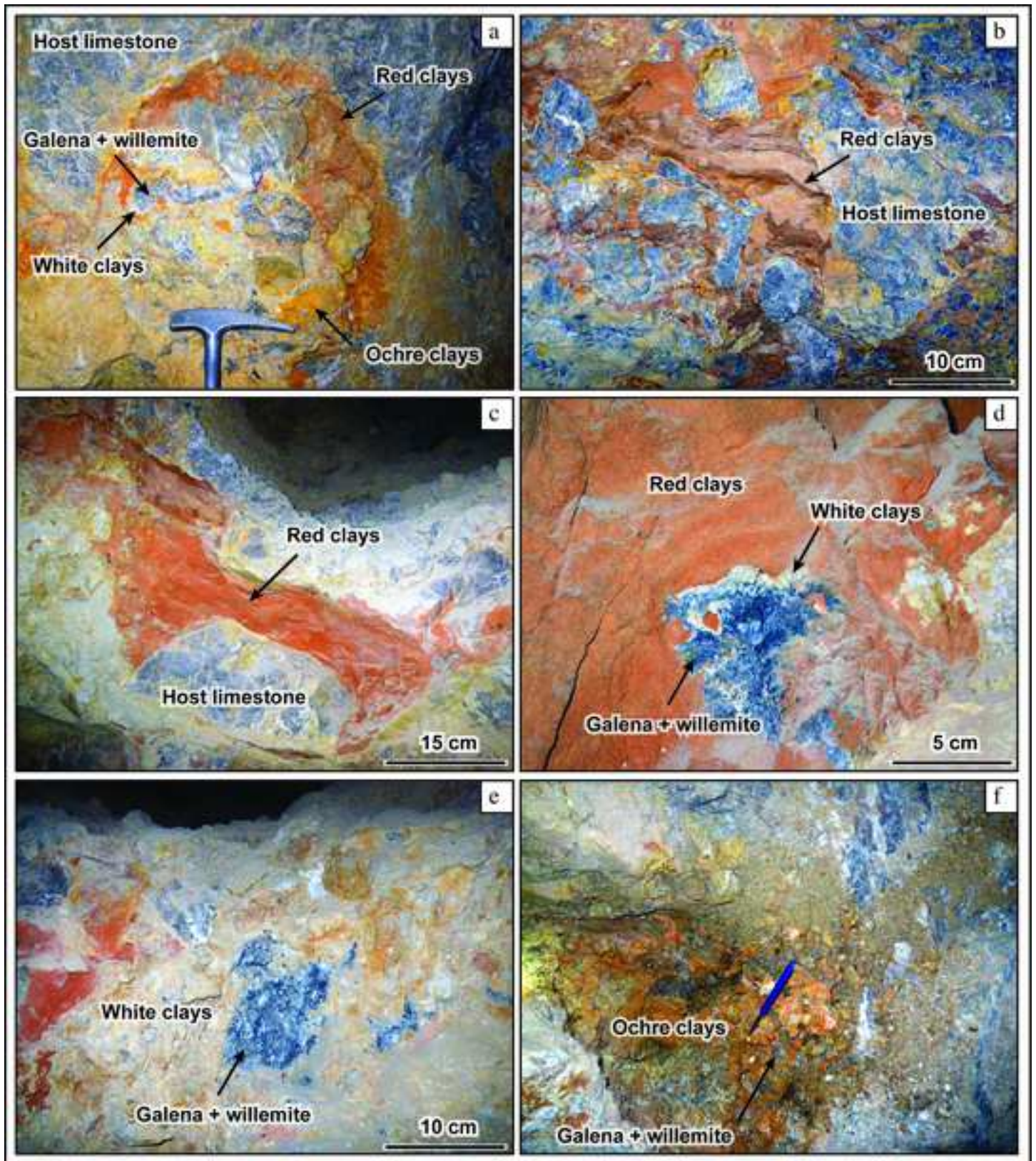


Figure 4
[Click here to download Figure: Fig4.tif](#)

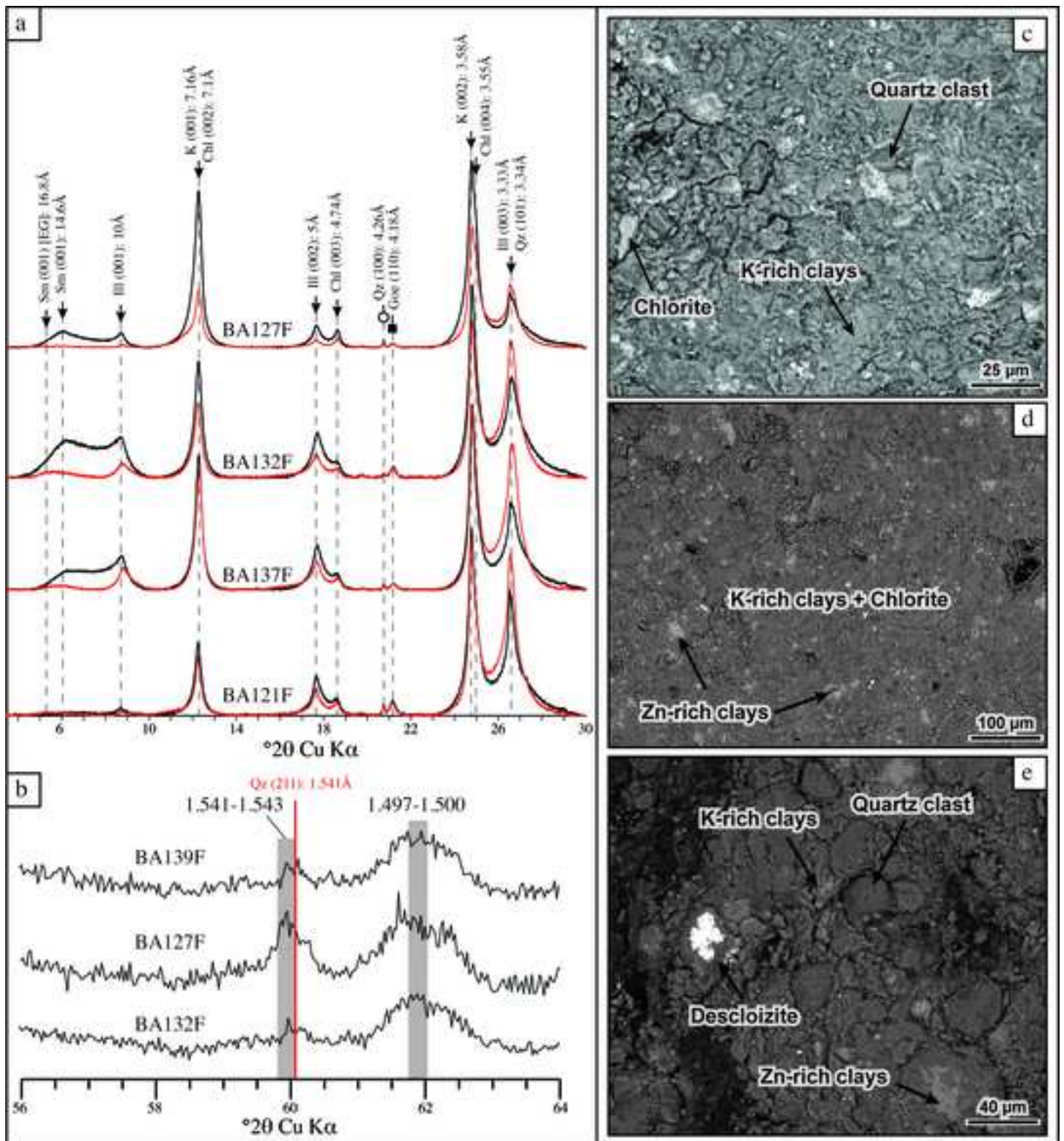


Figure 5
[Click here to download Figure: Fig5.tif](#)

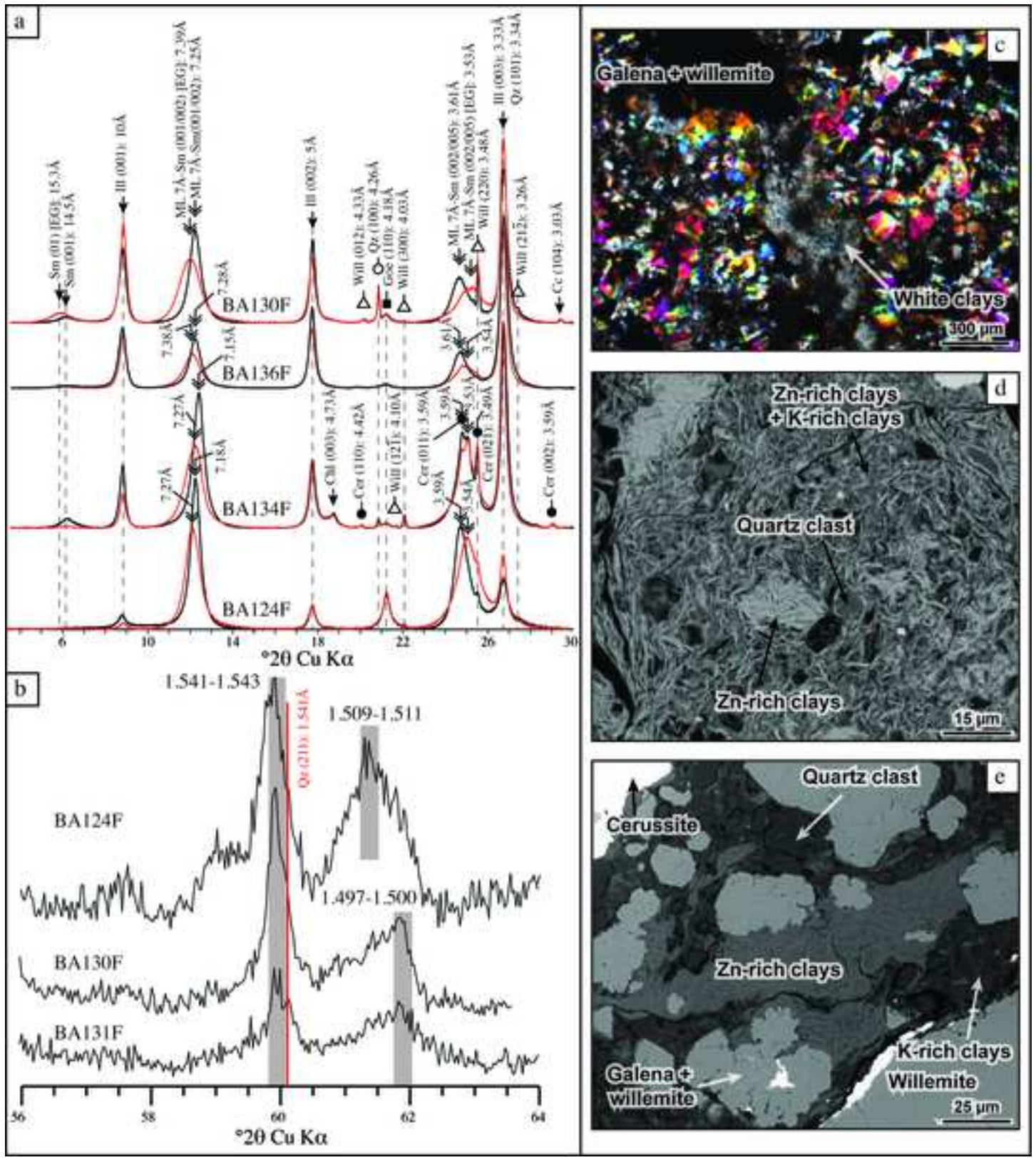


Figure 6
[Click here to download Figure: Fig6.tif](#)

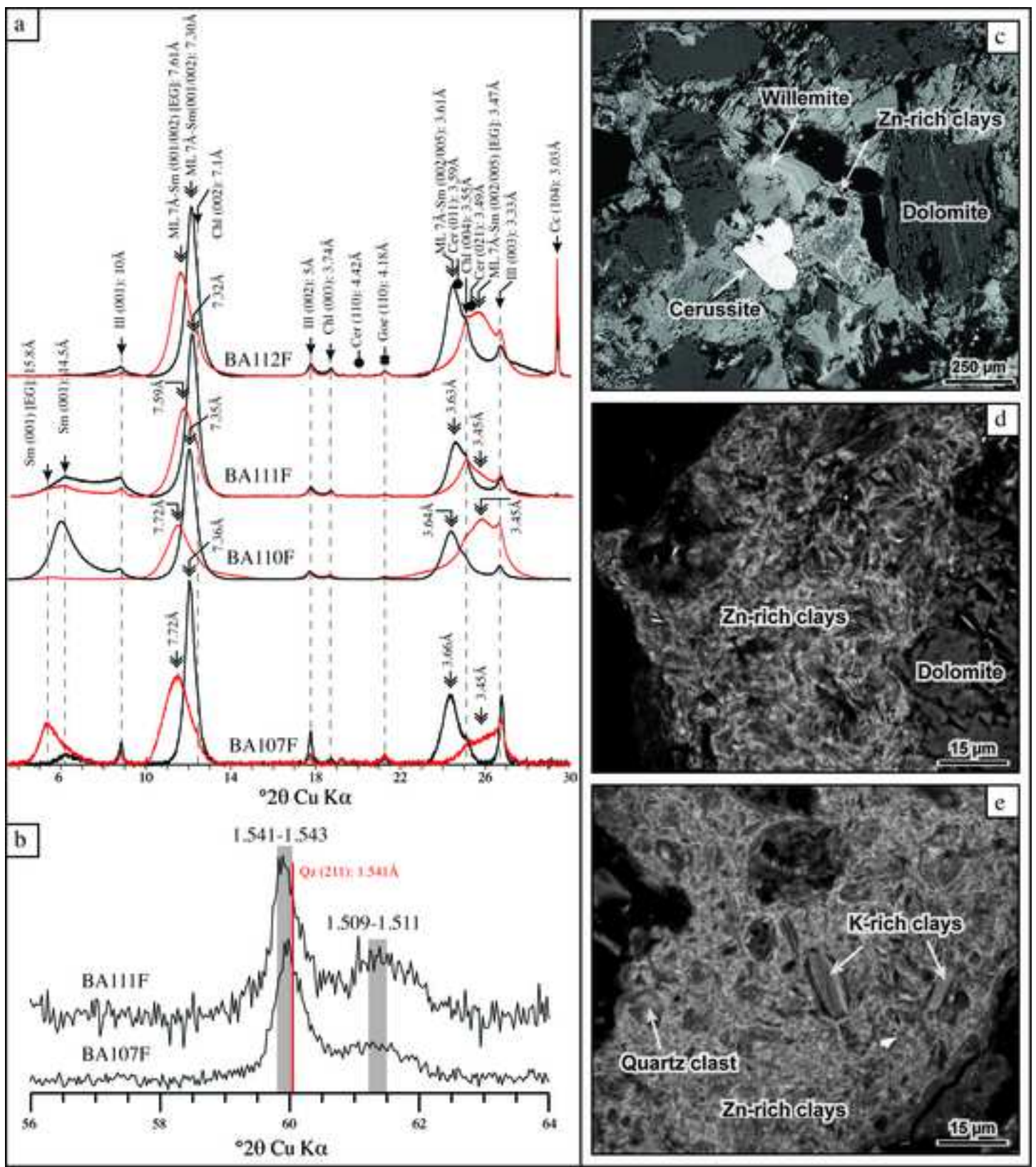


Figure 7
Click here to download Figure: Fig7.tif

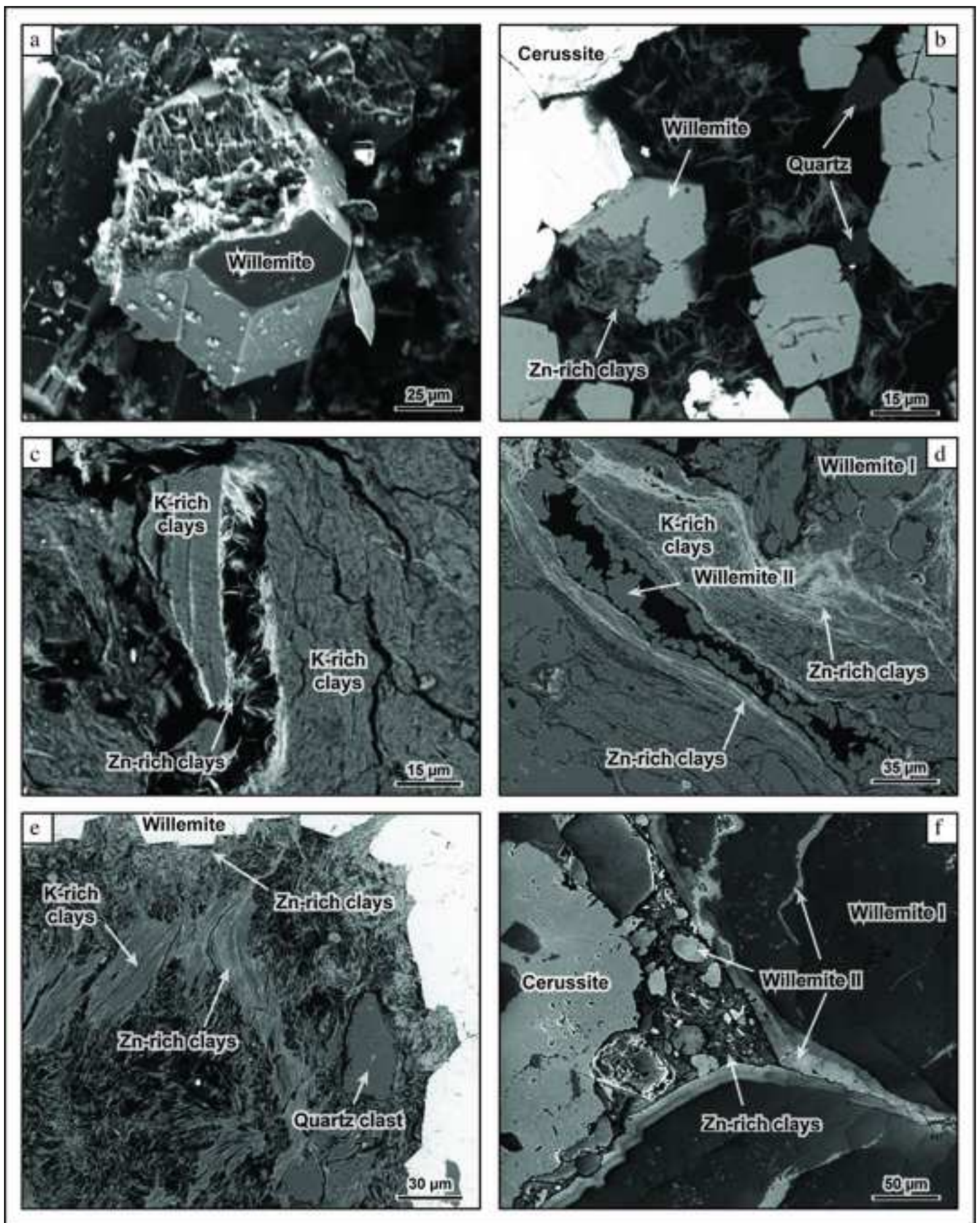


Figure 8
Click here to download Figure: Fig8.tif

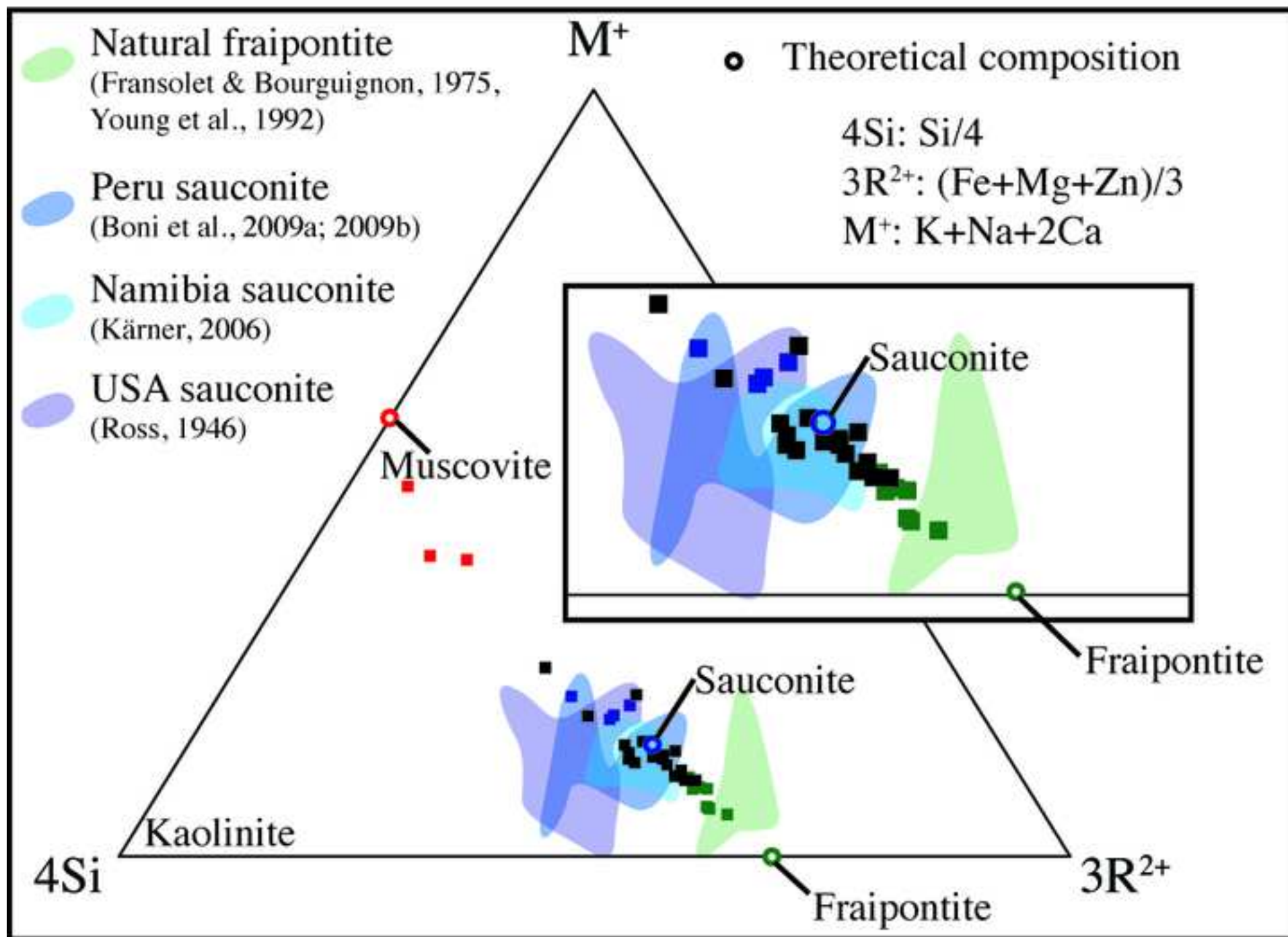


Figure 9

[Click here to download Figure: Fig9.tif](#)

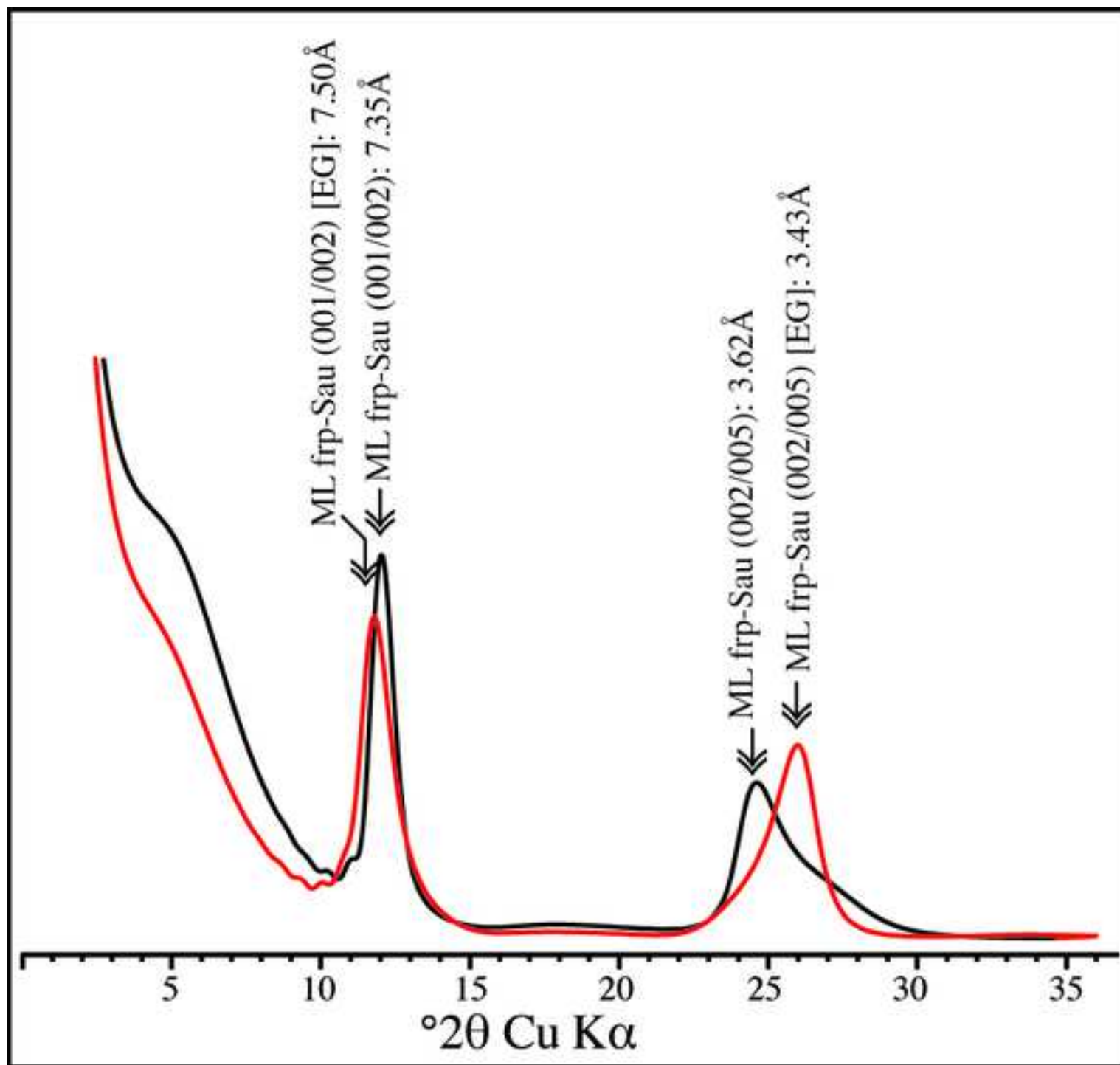


Figure 10
Click here to download Figure: Fig10.tif

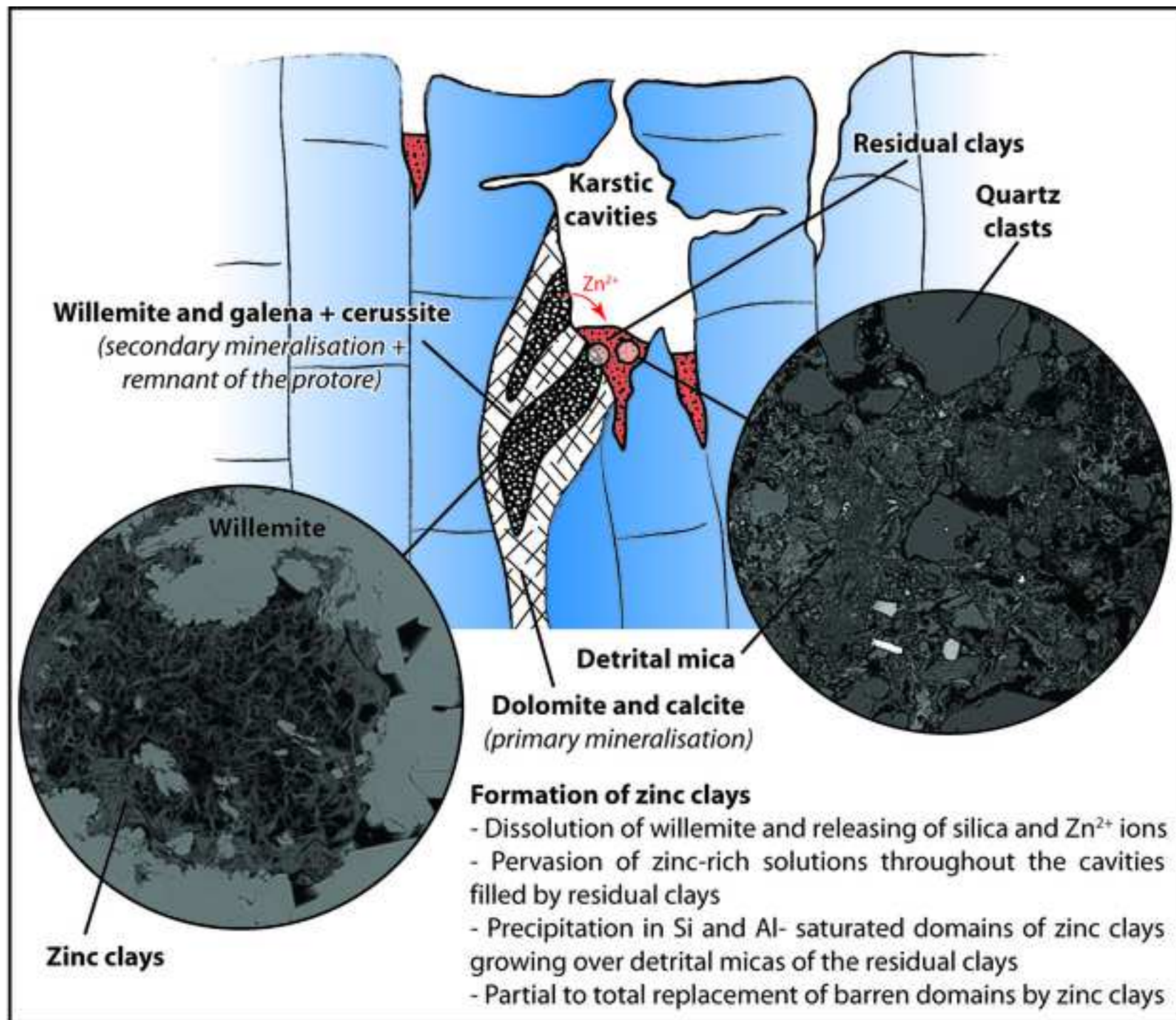


Table 1

Type	Sample	Mineralogy	LOI (%)	SiO2 (%)	Al2O3 (%)	Fe2O3 (%)	MgO (%)	CaO (%)	Na (%)	K2O (%)	MnO (%)	TiO2 (%)	P2O5 (%)	As (ppm)	Ba (ppm)	Cr (ppm)	Cu (ppm)	Ni (ppm)	Pb (ppm)	Sr (ppm)	Zn (ppm)	
Triassic clays																						
	BA125	qtz, cl, do, cc	20.98	31.83	8.73	4.53	8.83	19.33	0.14	0.94	0.08	0.57	0.15	119	115	49	60	50	90	160	51	1409
	BA139	qtz, cc, cl, goe	19.44	29.13	10.1	8.33	0.71	20.91	0.12	2.85	0.05	0.5	0.71	2177	71	163	293	85	27400	84	116	27600
	BA141	do, qtz, cl, cc, goe																				
	BA142	cl, qtz, goe, he, cc	6.04	45.3	14.1	24.57	1	0.81	0.1	4.38	0.06	0.73	0.31	726	136	70	166	28	9520	106	40	9672
	BA143	qtz, cl, he, do	6.1	59.98	12.15	8.12	7.58	1.07	0.0861	1.8	0.02	0.86	0.14	98	232	75	98	49	453	146	30	15000
	BA144	qtz, do, cl	13.6	45.66	11.58	6.2	11.92	6.34	0.0968	1.34	0.09	0.77	0.16	72	349	59	169	49	1020	152	34	19300
	BA149	qz, gy, cl	9.23	46.87	11.45	5.82	9.57	8.58	-	1.18	0.01	0.72	0.18	92	277	85	26	49	48	101	376	60
Jurassic rocks																						
	BA147	qtz, cc, cl, do	20.22	37.15	10.94	5.52	3.96	16.89	0.31	2.95	0.05	0.59	0.15	194	372	41	59	40	115	207	225	301
	BA148	cc, do, cl, qtz	34.68	17.19	1.94	1.92	1.04	40.88	0.0758	0.35	0.09	0.11	0.09	86	110	17	83	27	80	158	419	186
	BA148bis	cc, qtz, cl	34.8	17.18	2.06	1.93	1.08	40.43	0.0765	0.38	0.09	0.1	0.1	64	131	15	83	31	79	159	433	197
	BA150	cc, cl, do, qtz	41.76	3.79	0.92	1.73	6.11	43.91	-	nd	0.18	0.09	0.04	109	100	14	43	nd	148	100	83	392
	BA151	cc, do, cl, qtz																				
	BA152	do, cc, cl, qtz																				
	BA153	do, ce, qtz, cl, do, ga	27.06	14.8	2.29	0.94	2.46	25.86	-	0.13	0.05	0.16	0.11	306	108	31	218	nd	221200	66	219	25700
	BA154	qtz, cc, cl																				
	BA156	do, cc, cl, qtz	43.86	2.37	1.17	1.32	13.13	36.6	-	0.21	0.1	0.08	0.06	118	10	16	23	nd	941	80	145	2588
	BA157	cc, qtz, cl	25.15	29.56	7.82	3.07	h	27.7	-	1.98	0.04	0.5	0.12	159	105	39	98	40	157	147	299	214
	BA158	do, cc, cl	44.94	0.51	0.3	1.95	11.94	37.94	-	nd	0.14	0.02	0.07	109	70	11	52	nd	145	153	53	381
	BA159	do, cc, qtz, cl	37.13	10.01	4.97	2.19	6.71	35.78	-	1.1	0.34	0.29	0.14	34	424	29	37	54	919	142	83	403
	BA160	cc, qtz, cl, goe	26.41	30.36	5.27	6.5	0.44	28	-	1.01	0.09	0.4	0.16	141	79	38	97	nd	1400	111	118	919
			26.43	30.25	5.34	6.69	0.44	27.9	-	0.98	0.09	0.42	0.17	181	83	39	103	38	1349	115	120	937
Red clays																						
	BA101	qtz, cc, cl	15.25	50.62	6.31	3.43	0.33	16.54	0.15	0.57	0.06	0.85	0.17	82	93	61	261	214	526	120	91	830
	BA113	qtz, cl, do	3.89	77.06	7.78	5.57	0.83	0.97	0.11	0.84	0.1	0.8	0.1	83	126	61	114	72	753	142	40	3495
	BA115	qtz, cl	7.9	50.68	20.49	8.87	1.79	0.64	0.16	2.53	0.06	1.17	0.15	469	361	112	173	65	1657	46	110	8495
	BA116	qtz, cl, cc																				
	BA121	qtz, cl, goe	7.62	52.99	18.99	10.02	1.75	0.5	0.11	2.35	0.03	1.15	0.2	327	228	89	159	36	1732	51	96	30000
	BA126	qtz, cc, cl	7.15	73.49	3.38	1.79	0.17	7.95	0.1	0.31	0.05	0.45	0.1	274	488	40	98	42	1869	142	37	9352
	BA127	qtz, cc, cl	8.76	49.62	18.42	7.19	2.17	2.07	0.12	1.87	0.02	1.04	0.13	149	308	86	179	84	1214	88	115	47300
	BA132	qtz, cl, cc																				
	BA137	qtz, cl, cc, ce	8.21	62.24	14.48	6.1	1.44	3.57	0.0881	1.76	0.03	0.98	0.1	101	195	78	109	43	1097	140	76	6362
White Clays																						
	BA117	will, ce, cc, cl, qtz, do, ga																				
	BA118	ce, will, cl, qtz, cc, ga, do																				
	BA124	will, cl, ce, goe, qtz, cc	15.66	18.21	1.78	3.24	LD	20.89	0.0778	0.25	0.03	0.1	0.33	459	49	43	193	56	8094	210	47	322400
	BA128	will, cl, ce, ga																				
	BA130	qtz, will, cl, cc, do	9.13	47.32	5.36	2.08	0.92	8.32	0.21	1.17	0.02	0.34	0.24	1133	176	138	255	34	9218	101	53	180900
	BA131	qtz, cc, cl, will, do																				
	BA133	will, qtz, cl, do, cc																				
	BA134	will, ce, qtz, cl, ga																				
	BA135	will, cl, cc, qtz, ce, ga, goe																				
	BA136	qtz, cl, do, will, ce	25.86	29.94	6.95	1.43	10.36	16.97	0.0926	1.88	0.16	0.36	0.17	411	46	69	127	36	37100	138	237	17400
	BA138	will, cl, ce, qtz, ga																				
	BA145	do, ce, cl, qtz, ga																				
Ocher clays																						
	BA102	qtz, do, cl, dol	9.65	47.09	17.89	10.41	3.41	4.01	0.18	2.32	0.12	1.13	0.09	574	451	140	10848	117	3202	137	73	7748
	BA103	do, cc, cl, qtz																				
	BA104	cc, cl, do, qtz	15.57	31.13	14.94	7.99	2.96	11.46	0.18	1.87	0.18	1.14	0.11	586	8530	85	223	125	3321	182	161	64600
	BA107	cl, cc, do, qtz	14.02	26.12	9.6	7.93	2.66	7.58	0.14	0.85	0.12	0.71	0.11	389	84	58	401	180	1384	131	70	237000
	BA108	qtz, cc, cl, do	17.56	32.67	7.56	15.2	3.75	15.86	0.15	1.23	0.1	0.44	0.19	590	240	103	488	73	4273	72	68	27600
	BA110	do, cl, qtz, cc, ce	26.66	16.49	5.45	2.29	1.8	29.3	0.2	0.5	0.07	0.31	0.09	146	49	41	564	154	27100	149	135	92000
	BA111	cl, do, cc, qtz																				
	BA112	cc, cl, do, qtz																				
	BA114	qtz, cl, do, cc	7.64	59.21	18.52	4.69	1.36	0.68	0.16	1.75	0.04	1.38	0.13	88	237	114	135	66	949	57	111	21500
	BA119	cc, cl, ce, qtz, do	39.26	5.45	2.67	1	0.76	43.52	0.13	0.66	0.05	0.16	0.1	271	31	32	73	36	19440	51	315	6275
	BA123	qtz, cl, cc, do	8.59	53.29	20.17	7.88	1.95	1.73	0.14	2.21	0.08	1.1	0.14	195	263	100	100	48	2394	70	102	18400
	BA146	qtz, do, cl, cc	20	37.98	12.29	2.11	7.45	11.31	0.11	3.13	0.05	0.69	0.16	137	269	54	40	26	1598	161	58	7408

Table 2

Type	Clay content	Sample	CEC (meq/100g)	[Zn] (%) of the CEC
Red Clays	kaol > ill >> chl	BA121	34	40.873
	kaol >> ill (ML ill/sm) > chl	BA127	30	0.235
	kaol > ill (IS ill/sm) >> chl	BA132	35	0.167
	kaol > ill (IS ill/sm) >> chl	BA137	38	0.047
White Clays	White Clays			
	ML (7Å/sm) >> ill	BA124	13	1.555
	ill > ML (7Å/sm) >> sm	BA130	12	0.168
	ML (7Å/sm) > ill >> chl > sm (not presented)	BA131	27	0.121
	ill > ML (7Å/sm)	BA136	9	0.486
Ocher Clays	Ocher Clays			
	ML (7Å/sm) > sm >> ill	BA107	41	0.055
	ML (7Å/sm) > ill >> sm (not presented)	BA108	19	0.000
	ML (7Å/sm) > sm >> ill > chl	BA110	40	0.046
	ML (7Å/sm) >> sm > ill > chl	BA111	34	0.594

Table 3

	58	57	10	19	29	20	38	26	37	55	53	49	27	43			
Al ₂ O ₃	30,418	27,047	28,727	14,142	13,862	13,504	14,166	10,929	10,727	11,835	12,150	10,962	11,582	12,421			
SiO ₂	48,994	44,774	42,446	34,286	31,786	32,332	30,827	29,163	30,267	28,472	30,337	27,784	30,093	29,862			
MgO	1,661	1,659	0,696	1,220	0,909	1,455	1,042	0,598	0,783	0,732	0,719	0,617	0,571	0,639			
FeO	1,365	1,212	1,791	3,022	3,821	2,092	3,045	1,733	2,496	0,841	0,935	0,921	1,443	0,890			
CaO	0,136	0,169	0,304	0,669	0,550	0,778	1,053	0,789	0,830	0,535	0,506	0,451	0,646	0,472			
K ₂ O	10,005	7,477	6,333	2,286	1,954	1,756	1,526	0,220	0,400	0,612	0,668	0,172	0,054	0,290			
ZnO	1,860	12,984	8,316	24,677	28,583	31,004	31,929	45,455	43,963	46,668	46,254	49,392	48,535	48,882			
PbO	0,180	0,196	0,379	0,395	0,284	0,205	0,306	0,197	0,146	0,103	0,161	0,256	0,037	0,183			
Total	94,776	95,877	89,203	81,900	82,765	84,424	85,379	91,056	91,594	92,058	93,831	92,709	95,044	95,999			
	Micas (calculated on 110)			Sauconite (calculated on 110)					Frapionite (calculated on 140)								
Si	3,300	3,168	3,137	3,185	3,024	3,031	2,909	3,563	3,641	3,463	3,564	3,419	3,532	3,478			
Al(T)	0,700	0,832	0,863	0,815	0,976	0,969	1,091	0,437	0,359	0,537	0,436	0,581	0,468	0,522			
Al(O)	1,714	1,425	1,640	0,733	0,578	0,523	0,485	1,137	1,162	1,160	1,247	1,009	1,134	1,183			
Mg	0,167	0,175	0,077	0,169	0,129	0,203	0,147	0,109	0,140	0,133	0,126	0,113	0,100	0,111			
Fe	0,077	0,072	0,111	0,235	0,304	0,164	0,240	0,177	0,251	0,086	0,092	0,095	0,142	0,087			
Zn	0,092	0,678	0,454	1,692	2,007	2,145	2,225	4,100	3,904	4,190	4,011	4,487	4,205	4,203			
Ca	0,010	0,013	0,024	0,067	0,056	0,078	0,106	0,103	0,107	0,070	0,064	0,060	0,081	0,059			
K	0,860	0,675	0,597	0,271	0,237	0,210	0,184	0,034	0,061	0,095	0,100	0,027	0,008	0,043			
Pb	0,003	0,004	0,007	0,009	0,007	0,005	0,007	0,006	0,005	0,003	0,005	0,008	0,001	0,005			
ZT	4,000	4,000	4,000	4,000	4,000	4,000	4,000	4,000	4,000	4,000	4,000	4,000	4,000	4,000			
ZOc	2,053	2,353	2,289	2,839	3,025	3,040	3,104	5,529	5,461	5,571	5,481	5,713	5,582	5,589			
ZI	0,869	0,688	0,621	0,337	0,293	0,288	0,290	0,137	0,168	0,165	0,164	0,087	0,089	0,102			
ZCh(T)	-0,700	-0,832	-0,863	-0,815	-0,976	-0,969	-1,091	-0,437	-0,359	-0,537	-0,436	-0,581	-0,468	-0,522			
ZCh(O)	-0,179	0,131	0,217	0,411	0,627	0,603	0,694	0,196	0,084	0,303	0,208	0,435	0,298	0,361			
ZCh(I)	0,879	0,701	0,645	0,404	0,349	0,366	0,397	0,241	0,275	0,234	0,228	0,146	0,170	0,161			
	31	21	15	40	30	14	8	3	50	22	48	56	9	52	45	44	61
Al ₂ O ₃	11,268	11,430	8,227	9,586	11,714	12,228	11,835	11,218	12,275	14,723	20,423	15,514	13,779	12,885	13,088	15,033	16,004
SiO ₂	27,531	31,670	31,210	28,536	29,332	33,317	32,249	34,047	28,108	36,985	38,990	32,539	36,505	31,157	32,005	32,027	32,546
MgO	0,732	1,262	0,897	0,837	1,248	0,845	0,968	0,860	0,674	1,157	2,133	0,807	1,127	0,696	0,714	0,860	0,793
FeO	6,419	2,775	1,111	1,716	3,346	2,121	2,030	1,719	0,725	2,950	3,805	0,679	2,098	1,002	1,974	1,153	0,955
CaO	0,579	0,799	1,023	0,762	0,596	0,719	0,855	0,842	0,408	0,820	0,293	1,039	0,868	0,485	0,479	0,340	0,301
K ₂ O	1,185	0,799	0,419	0,271	1,105	0,901	1,114	0,657	0,938	1,833	3,874	2,103	1,198	1,106	0,995	1,528	1,726
ZnO	32,400	32,257	38,827	40,653	35,375	35,813	37,081	38,073	43,892	30,573	21,132	39,054	38,257	45,090	43,658	42,782	43,150
PbO	0,685	0,000	0,316	0,000	0,117	0,242	0,115	0,051	0,195	0,168	0,460	0,081	0,195	0,183	0,330	0,183	0,029
Total	82,403	82,421	83,625	84,317	84,510	86,185	86,247	87,468	88,989	90,477	91,870	93,782	94,025	94,729	95,262	95,744	97,420
	Mixture of mica, sauconite and/ or frapionite (calculated on 110)																
Si	2,833	3,085	3,140	2,915	2,893	3,076	3,017	3,119	2,736	3,157	3,087	2,850	3,070	2,820	2,799	2,855	2,783
Al(T)	1,167	0,915	0,860	1,085	1,107	0,924	0,983	0,881	1,264	0,843	0,913	1,150	0,930	1,180	1,201	1,145	1,217
Al(O)	0,199	0,397	0,116	0,069	0,255	0,407	0,322	0,330	0,144	0,639	0,992	0,452	0,436	0,195	0,348	0,231	0,396
Mg	0,112	0,183	0,135	0,127	0,183	0,116	0,135	0,117	0,098	0,147	0,252	0,105	0,141	0,094	0,112	0,095	0,101
Fe	0,552	0,226	0,093	0,147	0,276	0,164	0,159	0,132	0,059	0,211	0,252	0,050	0,148	0,076	0,084	0,147	0,068
Zn	2,461	2,319	2,883	3,065	2,576	2,441	2,560	2,574	3,154	1,927	1,235	2,525	2,375	3,013	2,760	2,874	2,723
Ca	0,064	0,083	0,110	0,083	0,063	0,071	0,086	0,083	0,043	0,075	0,025	0,097	0,078	0,047	0,032	0,046	0,028
K	0,155	0,099	0,054	0,035	0,139	0,106	0,133	0,077	0,116	0,200	0,391	0,235	0,128	0,128	0,170	0,113	0,188
Pb	0,018	0,000	0,008	0,000	0,003	0,006	0,003	0,001	0,005	0,004	0,009	0,002	0,004	0,004	0,004	0,008	0,001
ZT	4,000	4,000	4,000	4,000	4,000	4,000	4,000	4,000	4,000	4,000	4,000	4,000	4,000	4,000	4,000	4,000	4,000
ZOc	3,343	3,126	3,235	3,407	3,293	3,134	3,179	3,155	3,459	2,927	2,740	3,134	3,104	3,382	3,309	3,355	3,289
ZI	0,219	0,183	0,164	0,119	0,202	0,177	0,219	0,159	0,159	0,275	0,416	0,332	0,207	0,175	0,202	0,159	0,216
ZCh(T)	-1,167	-0,915	-0,860	-1,085	-1,107	-0,924	-0,983	-0,881	-1,264	-0,843	-0,913	-1,150	-0,930	-1,180	-1,201	-1,145	-1,217
ZCh(O)	0,884	0,649	0,586	0,883	0,842	0,675	0,679	0,639	1,063	0,493	0,472	0,720	0,645	0,958	0,964	0,941	0,974
ZCh(I)	0,283	0,266	0,274	0,202	0,265	0,248	0,304	0,242	0,202	0,350	0,441	0,430	0,285	0,222	0,234	0,205	0,243